energies

MDPI

Article

Optimal Sliding-Mode Control of Semi-Bridgeless Boost Converters Considering Power Factor Corrections

José R. Ortiz-Castrillón [1,2,3], Sergio D. Saldarriaga-Zuluaga [3], Nicolás Muñoz-Galeano [1,*], Jesús M. López-Lezama [1], Santiago Benavides-Córdoba [1] and Juan B. Cano-Quintero [1]

[1] Research Group on Efficient Energy Management (GIMEL), Department of Electrical Engineering, Universidad de Antioquia (UdeA), Medellín 050010, Colombia; jrobinson.ortiz@udea.edu.co (J.R.O.-C.); jmaria.lopez@udea.edu.co (J.M.L.-L.); santiago.benavides@udea.edu.co (S.B.-C.); bernardo.cano@udea.edu.co (J.B.C.-Q.)

[2] Department of Electronics and Telecommunications Engineering, Universidad de Antioquia (UdeA), Medellín 050010, Colombia

[3] Facultad de Ingeniería, Departamento de Eléctrica, Institución Universitaria Pascual Bravo, Calle 73 No. 73A-226, Medellín 050036, Colombia; s.saldarriagazu@pascualbravo.edu.co

* Correspondence: nicolas.munoz@udea.edu.co

Abstract: Sliding-mode control (SMC) is a robust technique used in power electronics (PE) for controlling the behavior of power converters. This paper presents simulations and experimental results of an optimal SMC strategy applied to Semi-Bridgeless Boost Converters (SBBC), which includes Power Factor Correction (PFC). As the main contribution, the optimal coefficients of the SMC strategy are obtained using two metaheuristic approaches, namely the Genetic Algorithm (GA) and Particle Swarm Optimization (PSO). The main objective is to obtain the sliding coefficients that ensure the best converter response in terms of the input current and output voltage, both during start-up and under disturbances (including changes in load, source, and references). The fitness function to be minimized includes two coefficients, namely the Integrative Absolute Error (IAE) and the Integral Time Absolute Error (ITAE), for both the input current and output voltage. These coefficients measure the converter's effort to follow the control references. The IAE penalizes errors during start-up, whereas the ITAE penalizes errors in the steady state. The tests carried out demonstrated the effectiveness of the GA and PSO techniques in the optimization process; nonetheless, the GA outperformed the PSO approach, providing sliding coefficients that allowed for a reduction in the input current overshoot during start-up of up to 24.15% and a reduction in the setting time of the output voltage of up to 99%. The experimental results were very similar when tuning with the GA and PSO techniques; nevertheless, tuning with the GA technique produced a better response in the face of disturbances compared to the PSO technique.

Keywords: genetic algorithm; non-linear control; particle swarm optimization; sliding mode control; semi-bridgeless boost converter

check for updates

Citation: Ortiz-Castrillón, J.R.; Saldarriaga-Zuluaga, S.D.; Muñoz-Galeano, N.; López-Lezama, J.M.; Benavides-Córdoba, S.; Cano-Quintero, J.B. Optimal Sliding-Mode Control of Semi-Bridgeless Boost Converters Considering Power Factor Corrections. *Energies* **2023**, *16*, 6282. https://doi.org/10.3390/en16176282

Academic Editor: Gianluca Brando

Received: 28 July 2023
Revised: 15 August 2023
Accepted: 18 August 2023
Published: 29 August 2023

Copyright: © 2023 by the authors. Licensee MDPI, Basel, Switzerland. This article is an open access article distributed under the terms and conditions of the Creative Commons Attribution (CC BY) license (https://creativecommons.org/licenses/by/4.0/).

1. Introduction

Sliding mode control (SMC) is a robust control strategy used in engineering to regulate the behavior of dynamic systems. This non-linear control technique is commonly used in power electronics (PE) devices due to its robustness and fast response in the face of disturbances, as well as changes associated with the feeding source, load, operation point, and equipment parameters [1,2]. The main advantage of SMC in comparison to the classical Proportional–Integral (PI) control is its inherent ability to handle uncertainties, disturbances, and nonlinearities in a more robust manner. Furthermore, the system is not limited to a single operating point. This condition allows for a wide control range in AC systems, where the signals of the current and voltages feature positive and negative values in the time function [3–9]. SMC research efforts are focused on DC/DC converters, where

references and signals are constant over time, or AC systems that are linearized around an operating point. This facilitates SMC design, since sliding coefficients can be found for these operating points [10–14]. Nonetheless, there is no clear methodology for finding the sliding coefficients in an AC system while considering the time variation of signals from its differential model.

Control design and tuning are aspects directly related to the efficiency of PE devices. Controllers are designed to provide a fast response with minimum overshoot, together with the ability to reject disturbances (robustness) [15–18]. In this context, choosing appropriate control and tuning methods enhances device performance, reduces implementation costs, and allows for the downsizing of components such as filters [19–22]. Finding the optimal tuning (regardless of the selected control) poses challenges for control engineers when it is necessary to control several variables under various conditions. In this context, the optimization of control tuning can be accomplished by employing metaheuristic techniques.

Metaheuristic techniques are computational problem-solving approaches usually inspired by natural processes, such as evolution, swarm behavior, and physical phenomena, that offer robust solutions to optimization challenges. Unlike traditional algorithms, a metaheuristic approach explores the solution space more broadly by employing iterative, heuristic-based strategies [23]. Genetic Algorithms (GAs) and Particle Swarm Optimization (PSO) are two widely explored metaheuristic approaches. GAs are evolutionary search techniques that use adaptability based on biological systems to optimize a given objective function subject to a set of constraints. They start with a randomly generated population that must pass through phases of selection, crossover, and mutation, in order to find new solutions of better quality [24,25]. GAs have been used for tuning non-linear controllers at their optimal operating points, as indicated in [26–29]. On the other hand, PSO is a metaheuristic approach inspired by the behavior of swarms of insects, flocks of birds, and schools of fish. Within PSO, every candidate solution is represented by a particle that must update its position and velocity in every iteration of the search [30–32]. PSO has also been applied to solve power electronic problems. In [33], the authors implemented a PSO approach to compute the best parameters of a resonant controller that was used to accurately inject compensation waveforms in a power quality application. In [34], PSO was used for the design of power electronic circuits, and the authors of [35] used PSO to improve the dynamic response and power quality of a distributed static synchronous compensator.

In PE converters, the control parameters are usually found by considering the device under a black box model in order to minimize a fitness function with decision variables such as voltages and currents [36,37]. In these applications, the main objective is to follow the references as accurately as possible, regardless of ripple, start-up, disturbances, or unexpected changes in equipment operation [38].

This paper uses a Semi-Bridgeless Boost Converter (SBBC) with clamped diodes as a controlled rectifier, with DC voltage control and Power Factor Correction (PFC) [39,40]. This PE device is composed of two boost converters operating independently in each half-cycle of the electrical grid. These converters are symmetrical; consequently, the control signal to actuate their switches can be the same. Additionally, their topology may have other functions to improve energy quality in accordance with international standards IEC 61.000-3-2 [41] and IEEE 519 [42], such as (1) a reduction in the total harmonic distortion in the converter's input current (THDi) [43] and (2) real PFC [44]. These functions can be included in the control design in order to reduce the filtering process during converter implementation [45]. The optimization process is carried out through co-simulation in OpenModelica-Python. In this case, the SBBC and its corresponding control are implemented in OpenModelica, while the optimization algorithm is implemented in Python. The Python interface was developed to capture and manipulate the variables of the converter's circuit provided by OpenModelica. The main motivation of this paper is to expand on the research works presented in [39,46,47]. In [39], the SBBC mathematical model was explained, showing in detail each converter's operational mode. Furthermore, a PI control was designed and implemented for the converter's input current and output voltage.

This system has a cascade control with an external loop to guarantee a stable DC output voltage and an internal loop to ensure that both PFC and THDi in the input AC current comply with international standards. In [46], a hybrid SMC-PI control was implemented in order to improve the PI control's performance. In the first stage, the PI internal loop for the current was changed using SMC; in the second stage, an adaptive hysteresis band was implemented instead of the PWM modulator. These changes increased the system's robustness and speed while improving energy quality due to the reduction in the THDi. In [47], SMC was implemented in the SBBC, and its design was depicted step by step. Additionally, a comparison between PI, hybrid PI–SMC, and SMC was conducted in order to determine the controller with the best behavior. The results demonstrated that SMC had the best control with great robustness during start-up, less overshoot, high PFC, low THDi, faster stabilization time, and good performance in the face of disturbances and changes in the converter's parameters. Basically, these research works focused on designing, comparing, and implementing control strategies to improve the dynamic behavior of the SBBC. Nonetheless, the aforementioned papers featured a limitation in common: the parameters of the PI control and sliding coefficients for SMC were found through empirical tuning instead of an optimization technique. In [47], the performance of the SBBC was improved with non-linear control (SMC); however, the optimal tuning for this control was not studied or implemented. The main purpose of this paper is, therefore, to fill this gap.

This work optimizes the control strategy of the SBBC presented in [47] where the authors demonstrated that the converter's switches can operate directly with SMC and AHB without any other modulation technique. The main contribution of this work is twofold: implementation and comparison of two metaheuristic techniques, namely GA and PSO, to find the SMC optimal tuning for the SBBC, including the validation with experimental results. It is worth mentioning that this implementation, to the best of the authors' knowledge, has not been reported in the specialized literature before. The main efforts and studies about this issue focus on the implementation of metaheuristics for tuning PI and SMC-PI controllers for PE devices with AC signals [35,48–50]. Nevertheless, the timeline reported in [39,46,47], along with this paper, present an SMC with fixed switching frequency as a better option than PI to control AC power electronic devices. The fitness function associated with the metaheuristic approaches was designed with two performance indexes: the Integral of Absolute Error (IAE), and the Integral of Time multiplied Absolute Error (ITAE), considering the sliding coefficients as decision variables.

This paper is organized as follows: Section 2 describes the SBBC modeling, Section 3 presents the optimization problem and describes the metaheuristics selected for its solution. Section 4 explains the results and analyses of the SBBC and its control in OpenModelica with the GA and PSO implemented in Python. Section 5 presents the SBBC operation with the optimized control with experimental results. Finally, Section 6 offers the conclusions of the paper.

2. Semi-Bridgeless Boost Converter with Clamped Diodes

The topology to optimize is an SBBC with clamped diodes, which is composed of two Boost converters, as indicated in Figure 1. The main function of the SBBC is to act as a controlled rectifier to feed a load (R), ensuring a regulated DC output voltage while guaranteeing PFC at the AC side. The SBBC is fed by an AC source (v_s). The first Boost converter operates in the positive half-cycle and is formed by an inductor (L_1), two diodes (D_1) and (D_4), a switch (Q_1), and a capacitor (C). The second one operates in the negative half-cycle and consists of an inductor (L_2), two diodes (D_2) and (D_3), a switch (Q_2), and a capacitor C.

Figure 2 illustrates the first two operating modes of the converter for the positive half-cycle. Figure 2a exhibits the operating mode 1 when switch Q_1 is closed. In this case, the input voltage (v_s) is positive while Q_1 is closed and D_4 is directly polarized. The input current (i_s) increases exponentially, storing energy in the inductor L_1. Simultaneously, C supplies power to the load (R), reducing the output voltage (v_c). Figure 2b depicts the

second operation mode. In this case, v_s is positive and Q_1 and Q_2 are open; moreover, D_1 and D_4 are directly polarized. v_s and the voltage induced in L_1 are added, and supply power to R and C. v_c increases exponentially, incrementing i_c; simultaneously, i_s is reduced.

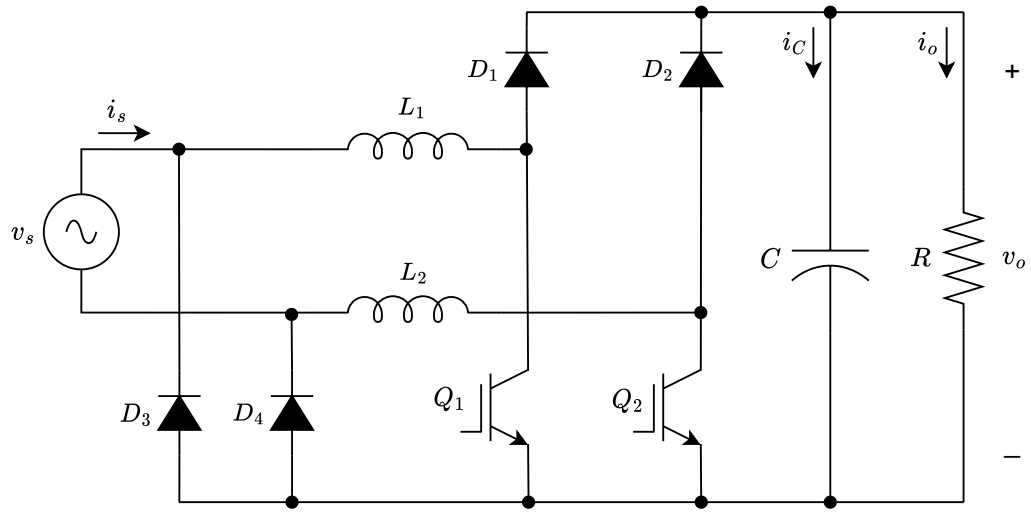

Figure 1. Semi-Bridgeless Boost Converter topology.

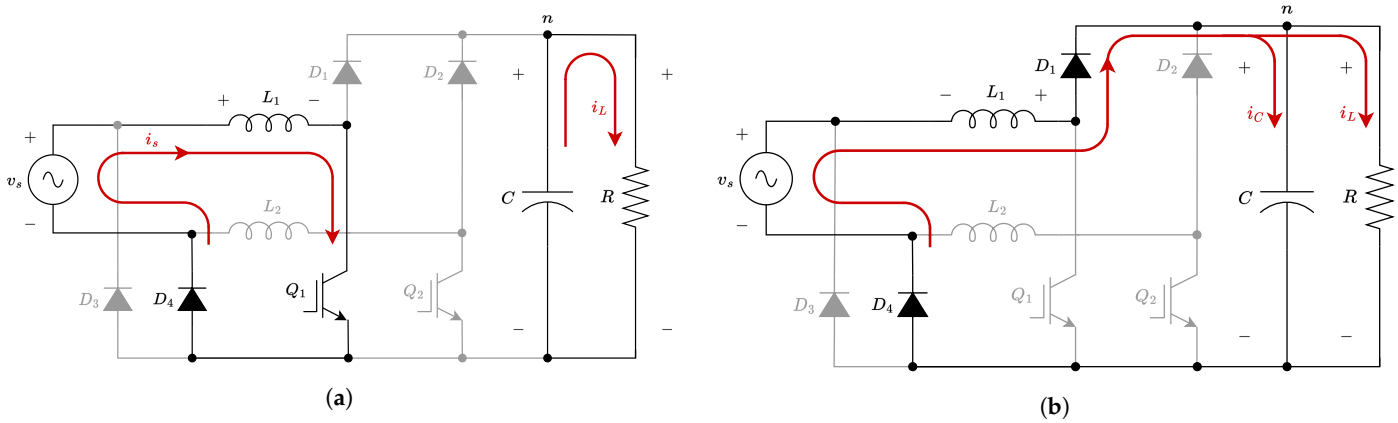

(**a**) (**b**)

Figure 2. Operating modes for the positive half-cycle. (**a**) Mode 1: Q_1 closed; (**b**) mode 2: Q_1 open.

Figure 3 shows the two operating modes of the converter for the negative half-cycle. Figure 3a depicts operating mode 3. In this case, v_s is negative and Q_2 is closed. Additionally, Q_2 and D_3 are directly polarized, and store energy in L_2. Simultaneously, C supplies power to R, reducing v_c. In operating mode 4 (Figure 3b), v_s is negative and Q_1 and Q_2 are open. Furthermore, D_2 and D_3 are directly polarized. In this case, v_s and the voltage induced in L_2 are added, supplying power to R and C.

Equations (1) and (2) describe the SBBC output voltage (v_o) and input current (i_s), respectively. The control variable (u) is the input signal to operate the power switches Q_1 and Q_2. Specific details in regard to SBBC modeling, deduction, and operation modes can be found in [39].

$$\frac{dv_o}{dt} = -\frac{v_o}{RC} + (1-u)\frac{i_s}{C} \tag{1}$$

$$\frac{di_s}{dt} = \frac{v_s}{L} - (1-u)\frac{v_o}{L} \tag{2}$$

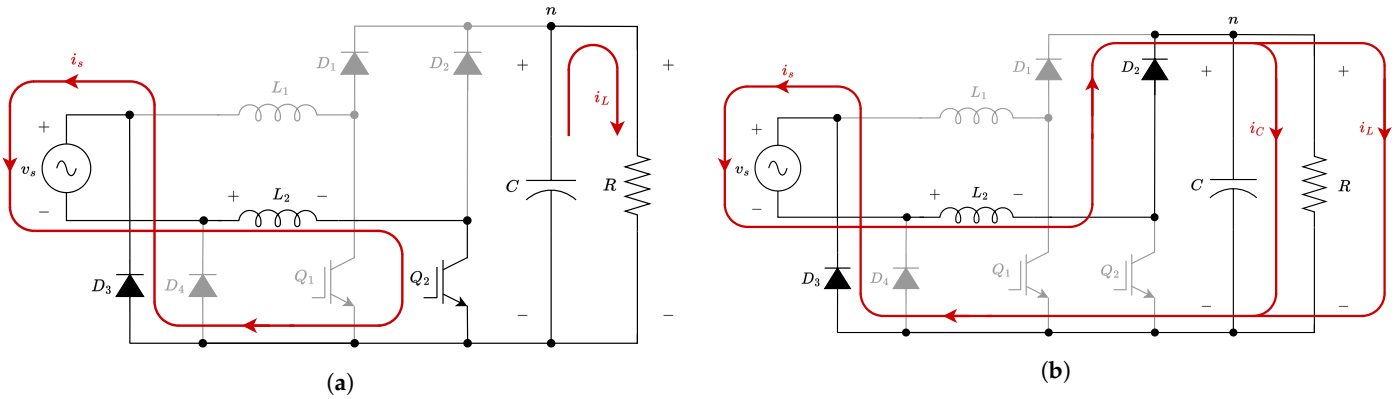

(**a**) (**b**)

Figure 3. Operating modes for the negative half-cycle. (**a**) Mode 3: Q_2 closed; (**b**) mode 4: Q_2 open.

The Adaptive Hysteresis Band (AHB) is given by Equation (3), where f_{sw} is the desired switching frequency and $|v_s| = V_{amp}|sin(\omega t)|$ is the rectified input voltage with V_{amp} as its amplitude. The rectification is considered because the SBBC has two converters, one for each half-cycle. The AHB sets the operating boundaries such as the bandwidth for the sliding surface. This band improves the energy quality. It reduces the zero crossing distortion of i_s, which causes issues in THDi in AC power electronic controllers. Detailed information on the design, mathematical modeling, and implementation of AHB (Equation (3)) in the SBBC and AC power converters is elaborated on in [46].

$$AHB = \frac{|v_s|(v_o - |v_s|)}{2Lf_{sw}v_o} \tag{3}$$

The sliding surface (S) used to control the SBBC is given by Equation (4), where α_1, α_2 and α_3 are the sliding coefficients. In this case, the first term (S_1) equates the normalized error of the output voltage that also allows to avoiding the non-minimum phase condition of boost converter topologies; S_1 is used to control v_o without using a cascade control that increases the system response speed. The second term (S_2) is the error of the input current used for PFC. The last term (S_3) is the integral of S_2 responsible of increasing the control robustness of the first overshoot in i_s during start-up. The sliding surface must comply with three conditions (transversality, existence, and equivalent control) based on the Lyapunov stability theorem to ensure control and system stability with the SMC. Detailed explanations and stability demonstrations of this sliding surface, given by Equation (4), as well as the SMC implementation, can be consulted in [47].

$$S = -\alpha_1 \underbrace{\left(\frac{v_o}{V_{ref}} - 1\right)}_{S_1} - \alpha_2 \underbrace{(i_s - i_{ref})}_{S_2} - \alpha_3 \underbrace{\int (i_s - i_{ref})dt}_{S_3} \tag{4}$$

The SBBC parameters used in this paper are presented in Table 1. The objective is to find the sliding coefficients for S where the controller has the best performance. Although the switching frequency may be high for this application it was selected for illustrative purposes based on previous works developed by the authors [47].

Table 1. Specifications of the SBBC

Parameter	Value
Grid voltage (v_s)	12 Vrms, 60 Hz
DC bus capacitor (C)	2200 µF
DC bus voltage (V_o)	30 V
Inductors ($L_1 = L_2 = L$)	2.2 mH
Switching frequency (f_{sw})	40 kHz
Load (R)	110 Ω

3. Optimization Process

This section describes the optimization model and the two metaheuristic techniques implemented for its solution.

3.1. Fitness Function and Constraints

The fitness function (labeled as ff) is proposed by adding the performance indexes IAE and ITAE for voltage and current, as shown in Equation (5) [51,52]. IAE penalizes errors in the start-up, while ITAE penalizes errors in the steady state. The Fitness Function (ff) is made of four terms, where W_i and W_v (with $W_i + W_v = 1$) are the weights associated with the input current (ff_i) and output voltage (ff_v), respectively. The minimization of ff improves the converter performance as follows: (1) it reduces the overshoot of the input current in the start-up, (2) the stabilization time is reduced for both input current and output voltage in the start-up and in face of disturbances or changes, and (3) it lowers the stabilization time for both input current and output voltage, despite changes in the operation point.

$$ff = \quad Min \quad \{W_i \underbrace{(IAE_i + ITAE_i)}_{ff_i} + W_v \underbrace{(IAE_v + ITAE_v)}_{ff_v}\} \tag{5}$$

Equation (6) defines ff_i as the sum of the IAE and ITAE for the input current as IAE_i and $ITAE_i$, respectively. Each index is represented by its discrete form, since the optimization process is performed with a data series (vectors) captured by Python from OpenModelica. The integral of the absolute value is calculated in using the trapezoidal method with the present error ($e_i(k)$) at instant k, and the previous error ($e_i(k-1)$) at instant $k-1$, being M the total of partitions and T_s the time delta. Each error is calculated with the measured and reference currents $e_i(k) = i_{med}(k) - i_{ref}(k)$ (at instant k) and $e_i(k-1) = i_{med}(k-1) - i_{ref}(k-1)$ (at instant $k-1$). The errors are calculated in the same way for IAE and ITAE. Nevertheless, the error in ITAE is multiplied by the time instant k. This means that, for longer periods, ITAE is more predominant than IAE.

Equation (7) defines ff_v as the sum of the IAE and ITAE for the output voltage as IAE_v and $ITAE_v$, respectively. In this case, the error calculations are similar to the one already described for the input current. The present error is defined as $e_v(k) = v_{med}(k) - v_{ref}(k)$, while the previous error is $e_v(k-1) = v_{med}(k-1) - v_{ref}(k-1)$.

$$ff_i = \left[\underbrace{\sum_{k=0}^{M} \left| \frac{e_i(k) + e_i(k-1)}{2} T_s \right|}_{IAE_i} + \underbrace{\sum_{k=0}^{M} k \left| \frac{e_i(k) + e_i(k-1)}{2} T_s \right|}_{ITAE_i} \right] \tag{6}$$

$$ff_v = \left[\underbrace{\sum_{k=0}^{M} \left| \frac{e_v(k) + e_v(k-1)}{2} T_s \right|}_{IAE_v} + \underbrace{\sum_{k=0}^{M} k \left| \frac{e_v(k) + e_v(k-1)}{2} T_s \right|}_{ITAE_v} \right] \tag{7}$$

According to [47], the fitness function is subject to the constraints given by Equations (8) and (9), these are evaluated with the values provided in Table 1. The constraints (8) and (9) ensure the stability of the controller in accordance with Lyapunov stability criteria.

$$\frac{\alpha_1}{\alpha_2} < \frac{2wCV_{ref}^2}{V_s} \Rightarrow \frac{\alpha_1}{\alpha_2} < 1.561 \tag{8}$$

$$\alpha_3 > 0 \tag{9}$$

All simulations were executed using an OpenModelica-Python interface, which allows reading and modifying data in OpenModelica through Python. The optimization process features six main steps: first, the function changes the sliding coefficients (decision variables) according to the metaheuristic criteria; second, it runs the simulation in OpenModelica; third, the variables of time, input current, output voltage, reference current and reference voltage are captured from the simulation; fourth, the performance indexes IAE_i and $ITAE_i$ for the current are calculated; fifth, indexes IAE_v and $ITAE_v$ for the output voltage are calculated; and finally, in the sixth step, the ff is computed in accordance with Equation (5).

3.2. Genetic Algorithm

Genetic Algorithms are techniques used to solve search and optimization problems inspired by the theory of evolution. These techniques have been widely used in control design and tuning [28,29,49]. Figure 4 shows the flowchart of the implemented GA. The main steps are described below.

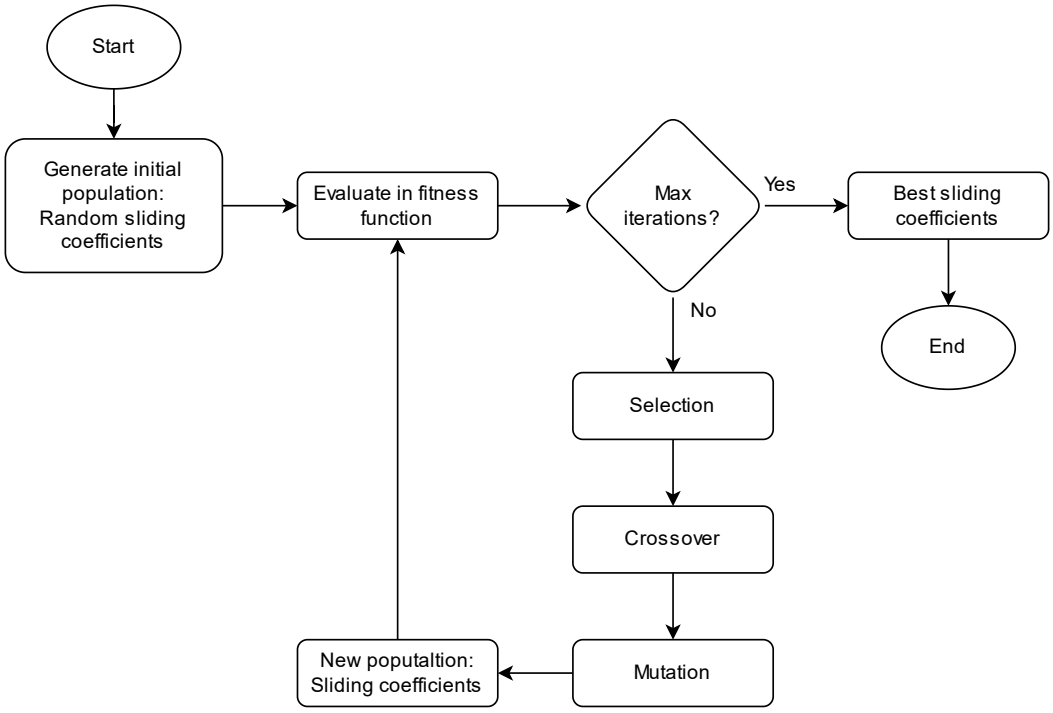

Figure 4. Flowchart of the implemented GA.

An individual or candidate solution to the problem is defined as a vector with the values $[\alpha_1, \alpha_2, \alpha_3]$. In the first step, the initial population is created using random values of these coefficients, considering the constraints indicated by Equations (8) and (9).

Then, the fitness function of each candidate solution is calculated, as indicated in Equation (5). The set of sliding coefficients that give the best results when the fitness function is evaluated; those that present the lowest error between the reference and the measured values after the simulation constitute the best candidate solutions, and could be selected to create new solution candidates.

In the selection step, the best candidate solution is chosen from a subset of randomly selected individuals from the current population (tournament selection). Every pair of winners of the tournament (parents) create two new solutions (offspring) through the crossover stage. The crossover or recombination stage is a binary operation in which two candidate solutions interchange information to create new individuals. In this step, the constraints given by Equations (8) and (9) are also considered.

The mutation step allows the GA to eventually escape from local optimal solutions, while the crossover or recombination stage gives intensification to the search process, the

mutation stage oversees diversification. In this case, the value of a sliding coefficient of the new candidate solution is randomly modified within its limits.

After the mutation step takes place, a new population of individuals is created. The new individuals (updated sliding coefficients) are changed in the circuit to repeat the simulation and obtain the measured new signals and a new iteration of the GA is started.

3.3. Particle Swarm Optimization

The codification of candidate solutions used in the PSO algorithm is the same one implemented for the GA. In this work, each particle in the population, which corresponds to a candidate solution, is defined by the vector of decision variables $x_i = [\alpha_1, \alpha_2, \alpha_3]$. The flowchart of the implemented PSO is illustrated in Figure 5.

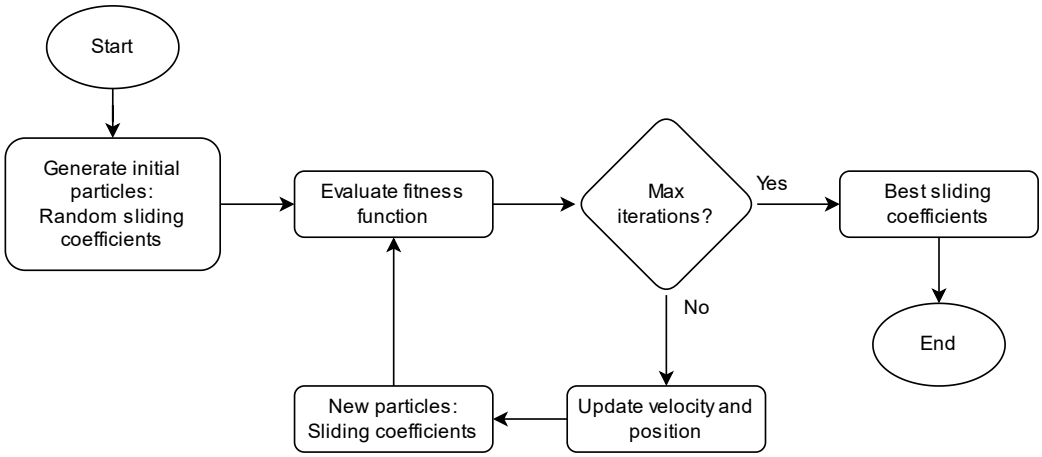

Figure 5. Flowchart of the implemented PSO.

The algorithm starts with a random generation of particles that are located within the search space. These particles must comply with the constraints given by Equations (8) and (9). Four characteristics are associated with each particle: a position representing a certain combination of values of the variables, the value of the objective function at the position where the particle is located, a velocity indicating how and where the particle is moving, and a record of the best position the particle has been to.

In every iteration, all particles must update their position and velocity using the expressions indicated in Equations (10) and (11) [53,54].

$$v_i(t+1) = w(t)v_i(t) + c_1 r_1 \left[x_{pBest_i} - x_i(t)\right] + c_2 r_2 \left[x_{pBest} - x_i(t)\right] \tag{10}$$

$$x_i(t+1) = x_i(t) + v_i(t+1) \tag{11}$$

where t indicates the number of the current iteration, $w(t)$ is the inertia weight, v_i is the velocity vector of the i-th particle, x_i is the position vector of the i-th particle, x_{gBest} is the vector corresponding to the best historical position of the whole swarm, and x_{pBest_i} is the vector equivalent to the best historical position of the ith particle. Finally, c_1 and c_2 are the personal and global learning coefficients, respectively.

4. Simulation and Optimization Results

This section presents the simulation and optimization processes along with the analyses of the main results. For both optimization techniques, the tuning of parameters was reached by trial and error. A population of 25 individuals was used for the GA, with crossover and mutation rates of 0.85 and 0.15, respectively. In regard to PSO, a population of 25 particles was used with an inertia weight of 1.0 and with global and personal learning coefficients of $c_1 = 1.5$ and $c_2 = 2$.

4.1. Circuit and Control Implementation in OpenModelica

Figure 6 shows the SBBC circuit to simulate in OpenModelica with the values from Table 1, according to the topology depicted in Figure 1. The total time of the simulation was 0.25 s; switches Q1 and Q2 are commutated by a control signal U.Q. The reference voltage is increased by 5% at 0.14 s and the load $R = 110\ \Omega$ is modified at 0.22 s by connecting a resistance in parallel with the same value. The measures Iin_T2 (input current) and Vo_T2 (output voltage), together with their respective reference signals, are the data exported to Python to compute the Fitness Function.

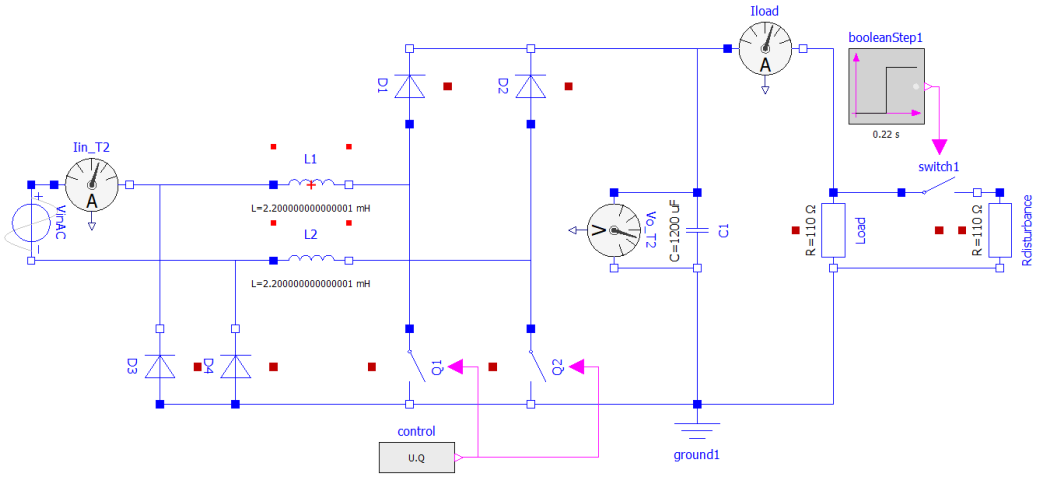

Figure 6. Semi-Bridgeless Boost Converter in OpenModelica simulator.

Figure 7 depicts the sliding surface where components S_1, S_2 and S_3 are calculated in agreement with Equation (4). In this case, blocks alpha1, alpha2 and alpha3 indicate the sliding coefficients ($\alpha_1 = 1$, $\alpha_2 = 1$ and $\alpha_3 = 1$); these are the decision variables that are imported and then exported when modified for each iteration of the metaheuristics coded in Python. In this case, the sliding coefficients are selected to evaluate and compare the sliding surface without modification with results after optimization.

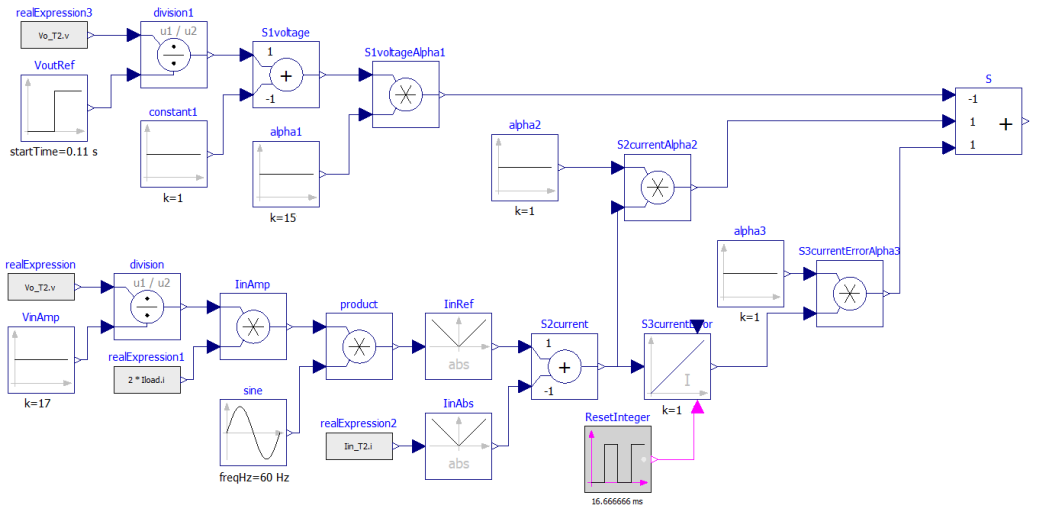

Figure 7. Sliding surface ($S = S_1 + S_2 + S_3$) in OpenModelica simulator.

Figure 8 shows the adaptive hysteresis band in OpenModelica, according to Equation (3). This band is built with measured signals and SBBC parameters.

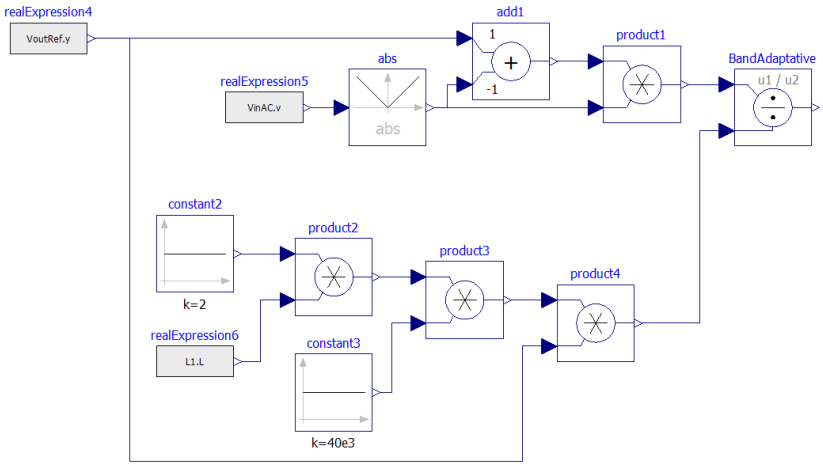

Figure 8. Adaptive hysteresis band in OpenModelica simulator.

Finally, the control signal is obtained by comparing the sliding surface with the adaptive hysteresis band, as indicated in Figure 9. This control has frequency limitation and operates the switches without any Pulse Width Modulation (PWM).

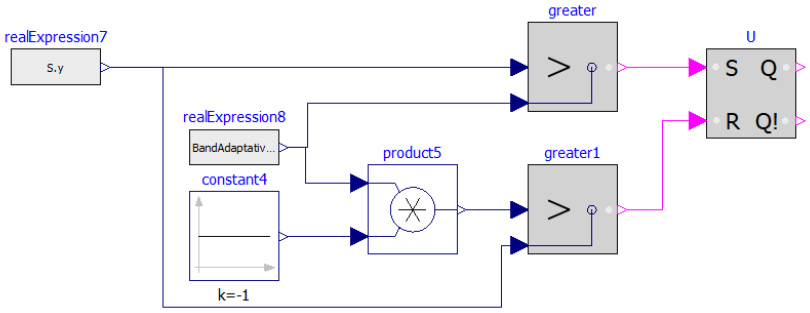

Figure 9. Controller in OpenModelica simulator.

4.2. Simulation Results without Optimization

Simulation results without optimization of the input current and its reference are shown in Figure 10. The input current presents an overshoot that reaches a maximum value of 11.18 Amperes in the start-up and stabilizes at 0.008 s. The zoom in the figure shows the time window (from 0.14 s up to 0.22 s) when both disturbances appear (there is an increment in the output voltage reference and the load is doubled). The change in voltage reference increases the input current amplitude (without overshoot) reaching its reference at 0.15 s. The load change only causes an instantaneous change in the amplitude of the current (without overshoot) and the reference is followed satisfactorily.

Simulation results without optimization of the output voltage and its reference are shown in Figure 11. Note that the output voltage does not present any overshoot in the start-up and stabilizes at 0.043 s. The zoom in Figure 11 indicates the time window from 0.14 s to 0.22 s (the same conditions were analyzed in the input current). The new voltage reference is reached at 0.172 s (without undershoot or overshoot); the system does not exhibit non-minimum behavior, and the load change increases the ripple.

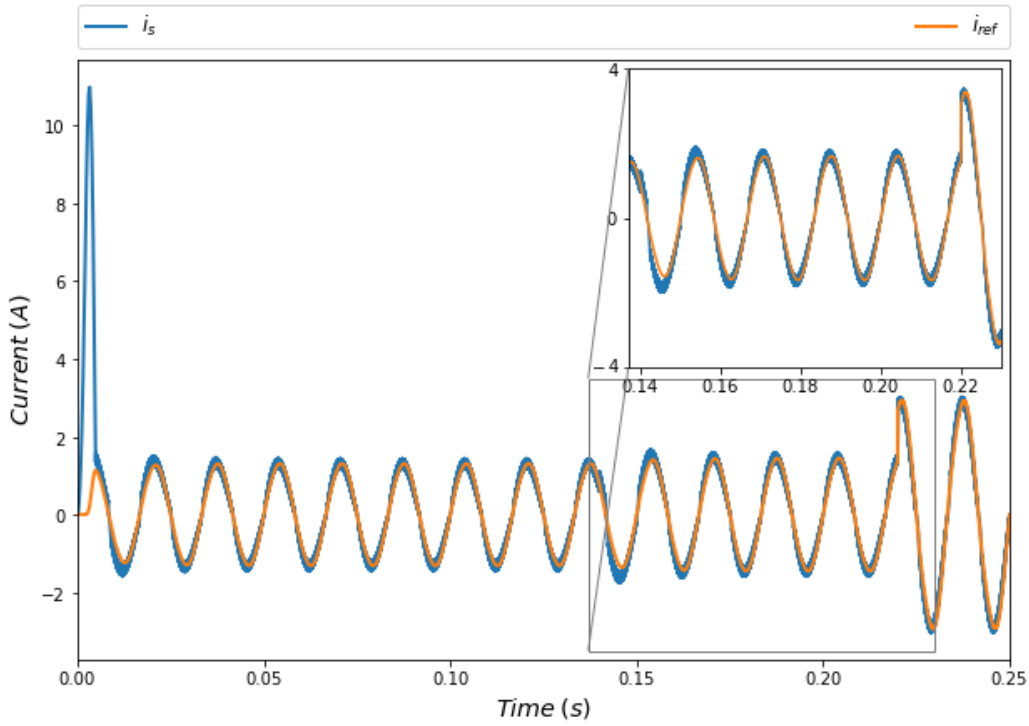

Figure 10. Simulation results in OpenModelica without optimization (input current).

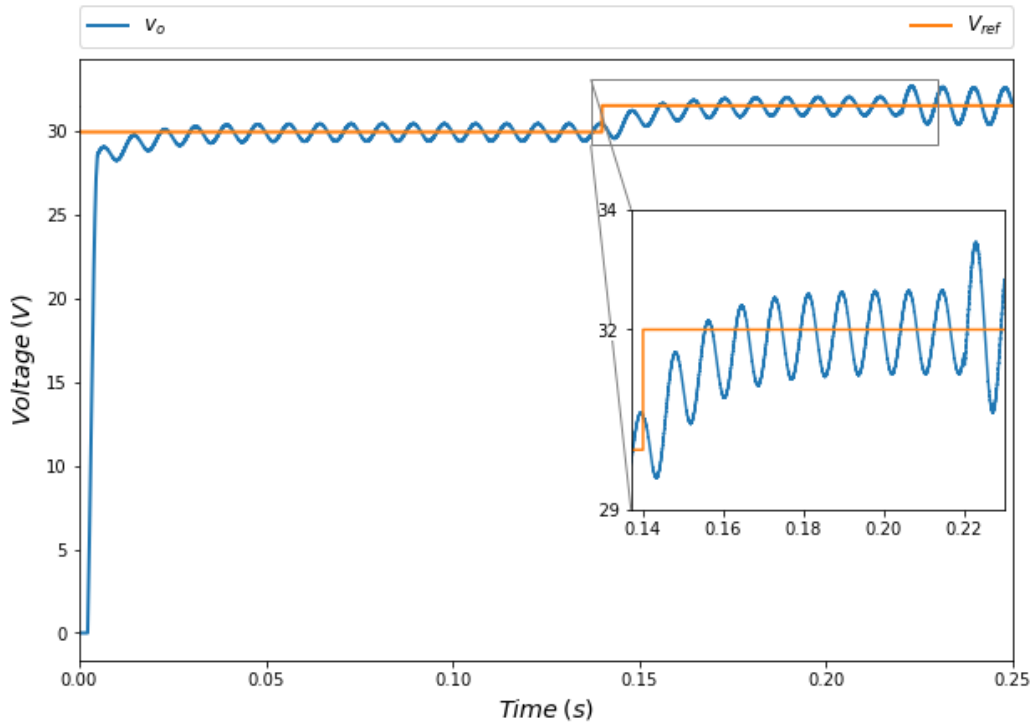

Figure 11. Simulation results in OpenModelica without optimization (output voltage).

4.3. Genetic Algorithm Implementation Results

Figure 12 depicts the convergence of the GA. In this case, weights $W_i = 0.85$ and $W_v = 0.15$ were selected to give more weight to the current because of its greater overshoot during start-up (see Figure 10). Note that the Fitness Function rapidly decreases and reaches convergence in about 14 iterations (from 4.831 to 3.764). In this case, the sliding

coefficients in the best operation point for the SBBC (best solution found) are $\alpha_1 = 10.65$, $\alpha_2 = 1.5$ and $\alpha_3 = 12.7$.

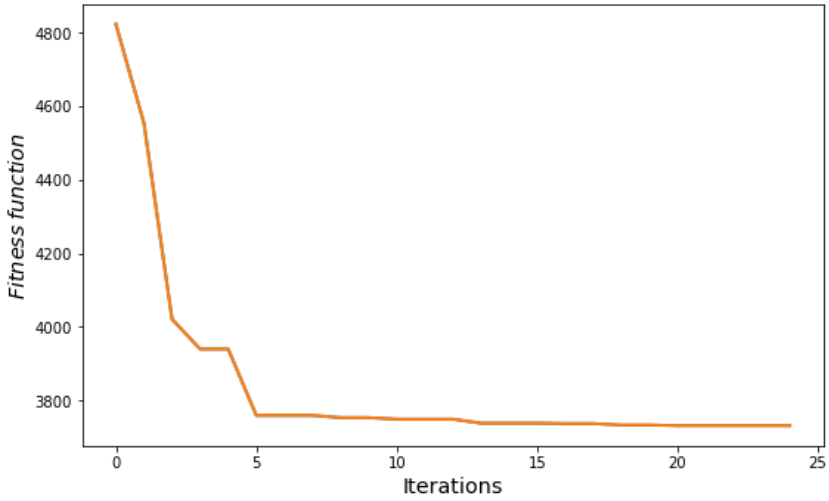

Figure 12. Convergence of the implemented GA.

Figure 13 illustrates the evolution of the performance indexes corresponding to the input current in each GA iteration. Figure 13a shows IAE_i, while Figure 13b depicts $ITAE_i$. It is observed in Figure 13a that there is an important reduction in the IAE_i that starts at 3362 and ends at 3141 when the GA converges. Similarly, the $ITAE_i$ presents initial and final values of 117.6 and 108.5, respectively, as exhibited in Figure 13b. It is worth noting that the indexes are not at their minimum value when the GA converges. However, the fitness function is at its minimum value (Figure 13b) finding the balance between current and voltage.

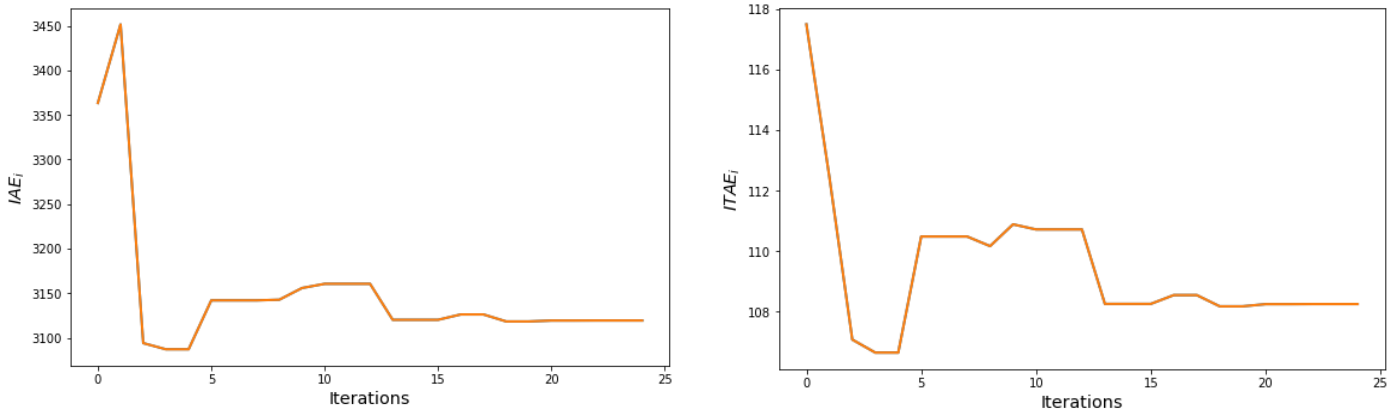

(**a**) (**b**)

Figure 13. Results of the input current performance indexes in each GA iteration. (**a**) Input current: IAE_i vs. iterations; (**b**) input current: $ITAE_i$ vs. iterations.

Figure 14 presents the simulation results with and without optimization for the input current (Figure 14a) and its absolute error (AE_i) (Figure 14b) with its evolution over time. As seen in Figure 14a, the initial overshoot of the current is reduced from 11.18 to 8.48 Amperes. Furthermore, the zoom in this figure shows a reduction in the transitory when the voltage reference is changed, and a similar response is obtained when the load is doubled. Figure 14b shows a reduction in the absolute error in the start-up and the zoom also evidences an important reduction in the error in the face of disturbances.

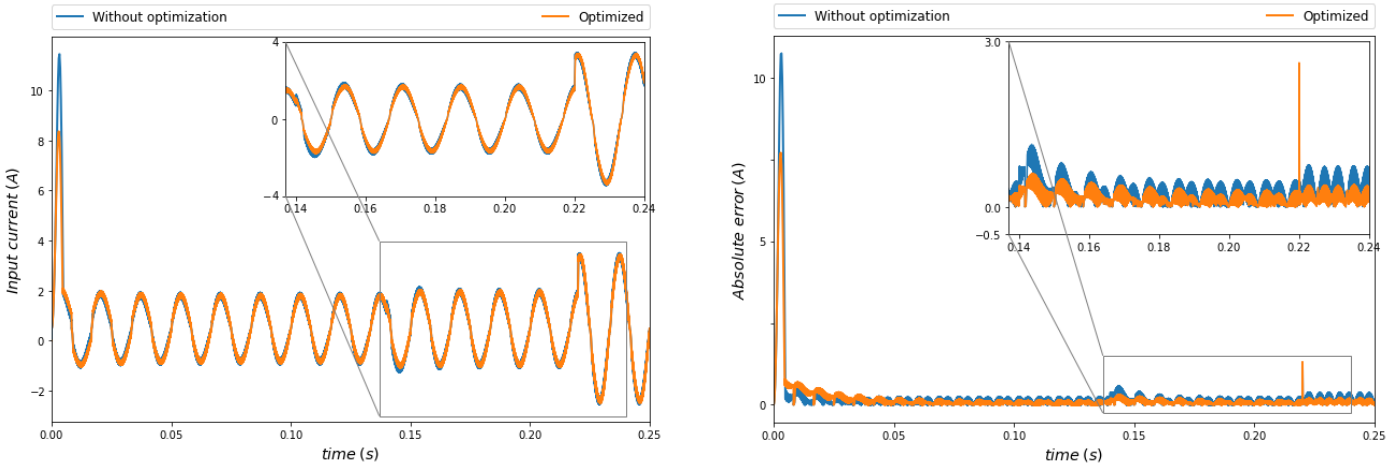

(**a**) (**b**)

Figure 14. Optimization results of the input current. (**a**) Input current before and after optimization; (**b**) current absolute error before and after optimization.

Figure 15 illustrates the performance indexes of the output voltage in each GA iteration. Figure 15a shows IAE_v, while $ITAE_v$ is depicted in Figure 15b. A reduction in IAE_v from 16,222 up to 8121 is observed in Figure 15a. The $ITAE_v$ also presents a significant reduction, starting at 511 and reaching 264, as indicated in Figure 15b.

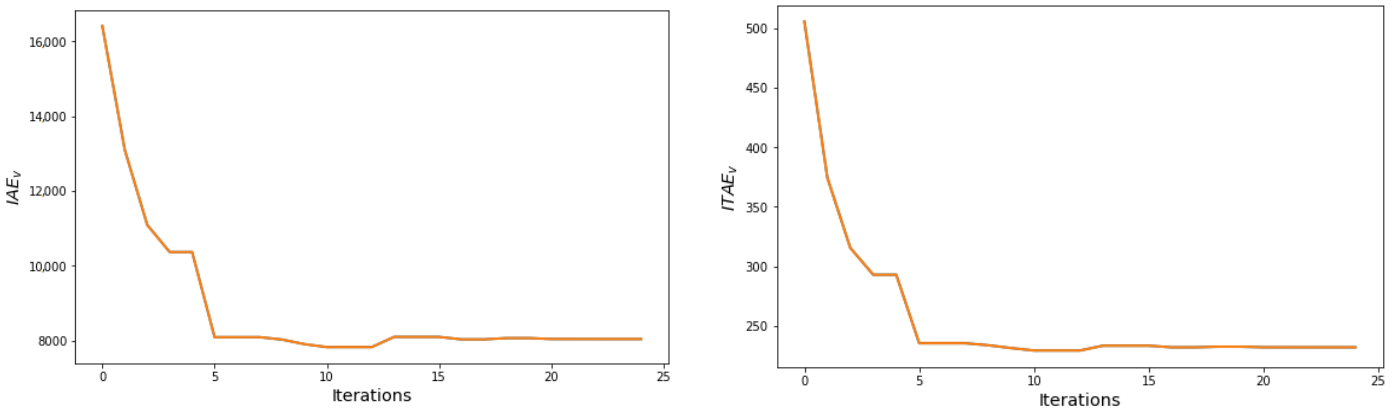

(**a**) (**b**)

Figure 15. Results of the output voltage performance indexes in each GA iteration. (**a**) Output voltage: IAE_v vs. iterations; (**b**) output voltage: $ITAE_v$ vs. iterations.

Figure 16 presents the simulation results with and without optimization of the output voltage (Figure 16a) and its absolute error (IAE_v) (Figure 16b) with its evolution over time. As seen in Figure 16a, there is an important reduction in the stabilization time, passing from 0.43 s to 0.0042 s with a small overshoot (2.6%). The zoom also evidences the same time to reach the new voltage reference. Figure 16b shows a reduction in the absolute error in start-up and disturbances.

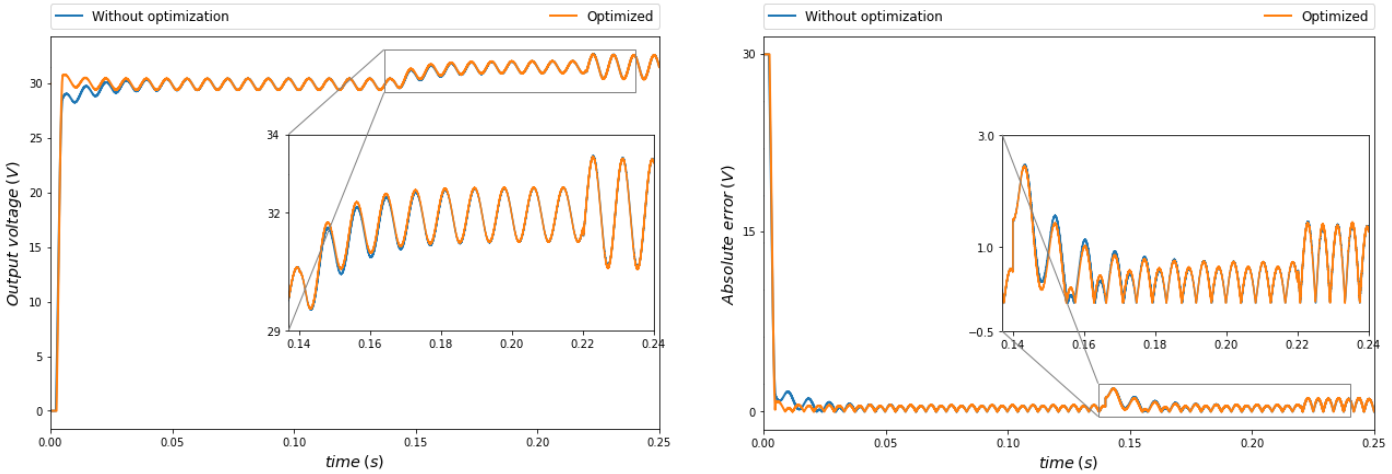

(**a**) (**b**)

Figure 16. Optimization results of the output voltage. (**a**) Output voltage before and after optimization; (**b**) voltage absolute error before and after optimization.

4.4. Particle Swarm Optimization Results

Figure 17 depicts the convergence of the PSO. In this case, weights $W_i = 0.8$ and $W_v = 0.2$ were selected to prioritize the current, as it presents a great overshoot during start-up. These weights are different from the ones used with the GA because for the same weights, the PSO reduced the current overshoot up to 60%, but the voltage did not reach the reference, i.e., the two objectives (for voltage and current) were not met at the same time. As shown in Figure 17, the Fitness Function reaches convergence in about 15 iterations starting at 4.500 and reaching 4.400. In this case, the convergence took more iterations compared to the GA. The sliding coefficients in the best operation point for the SBBC are $\alpha_1 = 13.21$, $\alpha_2 = 1.24$ and $\alpha_3 = 5.34$.

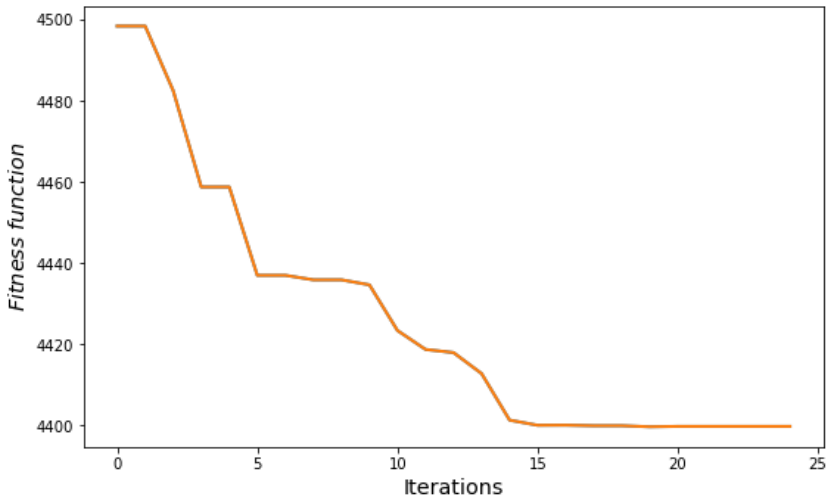

Figure 17. Convergence of the implemented PSO.

The evolution of the performance indexes corresponding to the input current in each PSO iteration is illustrated in Figure 18. Figure 18a shows IAE_i, while Figure 18b depicts $ITAE_i$. As observed in Figure 18a, IAE_i starts at 3294 and is reduced up to 3235 when the PSO converges. Likewise, $ITAE_i$ passes from 113.9 up to 109.1, as illustrated in Figure 18b.

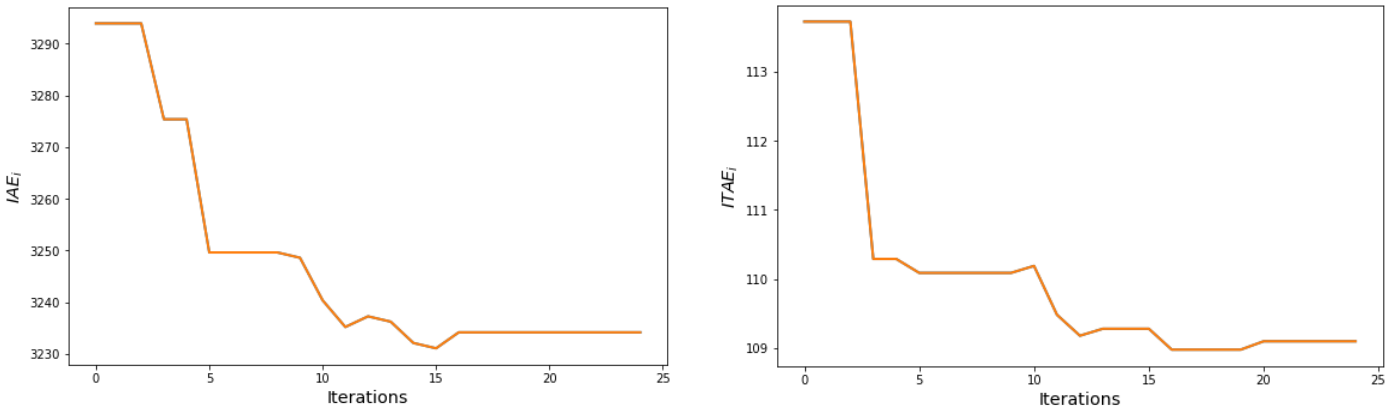

(**a**) (**b**)

Figure 18. Results of the input current performance indexes in each PSO iteration. (**a**) Input current: IAE_i vs. iterations; (**b**) input current: $ITAE_i$ vs. iterations.

Figure 19 presents the simulation results with and without optimization for the input current (Figure 19a) and its absolute error (AE_i) (Figure 19b), along with its evolution over time. As seen in Figure 19a, the initial overshoot of the current is reduced from 11.18 to 9.5 Amperes. The zoom in this figure shows a reduction in the transitory when the voltage reference is changed, and a similar response is obtained when the load is doubled. Figure 19b shows a reduction in the absolute error in the start-up, and the zoom also evidences a reduction in the error in the face of disturbances.

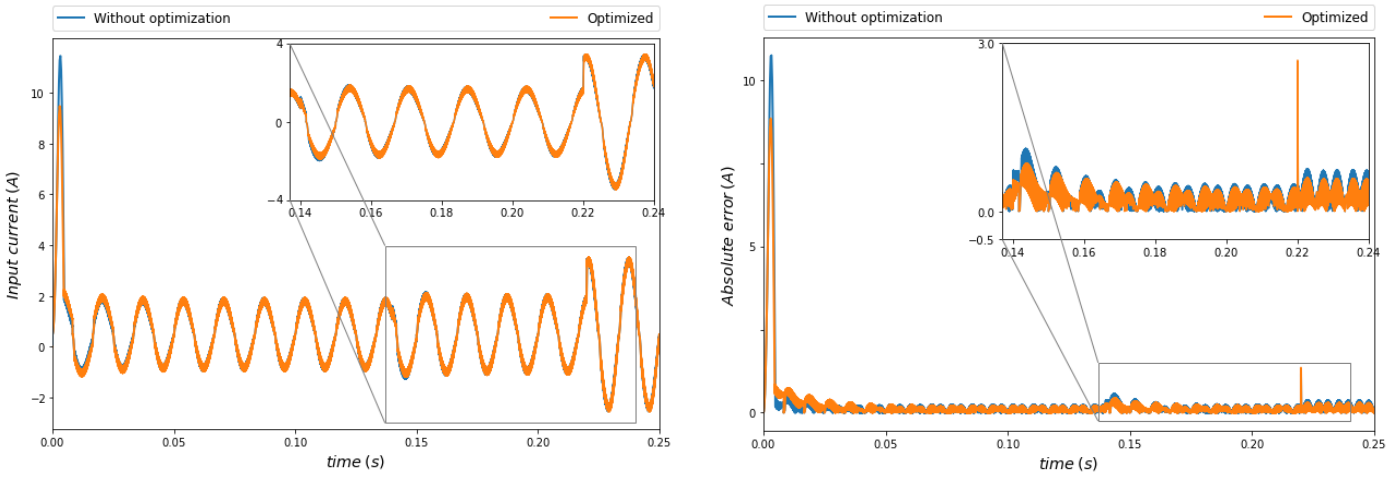

(**a**) (**b**)

Figure 19. Optimization results of the input current (PSO). (**a**) Input current before and after optimization; (**b**) current absolute error before and after optimization.

Figure 20 presents the performance indexes of the output voltage in each PSO iteration. Figure 20a shows IAE_v while $ITAE_v$ is depicted in Figure 20b. As observed in Figure 20a, there is a reduction in IAE_v from 8560 up to 8327. The $ITAE_v$ also reflects a reduction from 295.4 to 287.5, as illustrated in Figure 20b.

Figure 21 presents the simulation results with and without optimization of the output voltage (Figure 21a) and its absolute error (IAE_v) (Figure 21b) with its evolution over time. As seen in Figure 21a, the stabilization time is approximately the same, while the voltage continues without overshoot. The zoom also evidences that the behavior despite disturbances does not change. Figure 21b shows a reduction in the absolute error only in start-up.

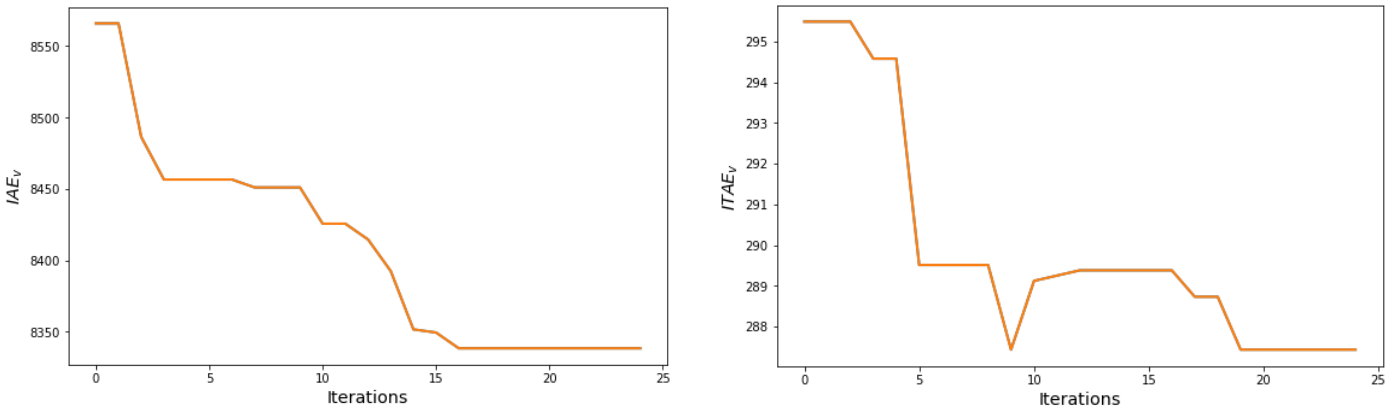

(**a**) (**b**)

Figure 20. Results of the output voltage performance indexes in each PSO iteration. (**a**) Output voltage: IAE_v vs. iterations; (**b**) output voltage: $ITAE_v$ vs. iterations.

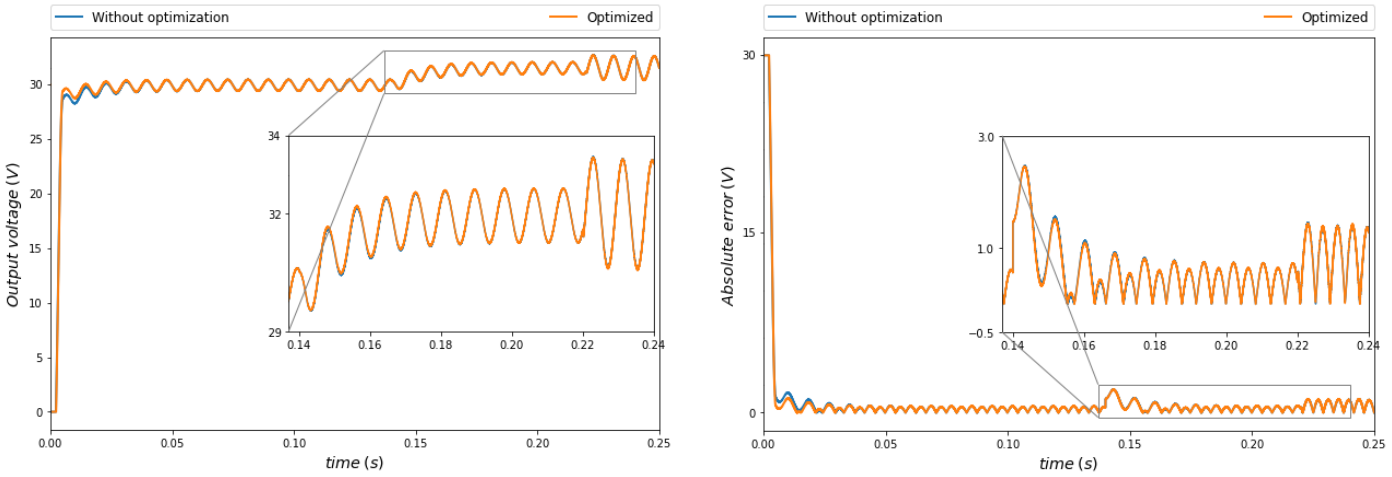

(**a**) (**b**)

Figure 21. Optimization results of the output voltage (PSO). (**a**) Output voltage before and after optimization; (**b**) voltage absolute error before and after optimization.

4.5. Simulation and Optimization Results: Comparison and Summary

The results evidenced that the optimization objectives were achieved with a reduction in the current overshoot and the stabilization of the output voltage in the start-up for both GA and PSO. Furthermore, the controller response was improved in the face of disturbances. In this case, load and reference changes. A summary of the most relevant results is provided in Table 2. The optimization results are compared with the values before optimization (original system). The two columns on the right show the percentage reduction for all analyzed and optimized variables: (1) For the input current, there is a 24.15% reduction in the over-peak with GA and 15% with PSO. IAE_i was reduced 6.6% with GA and 3.8% with PSO. $ITAE_i$ was reduced by 7.7% with GA and by 7.2% with PSO; (2) For the output voltage, there was a reduction in the stabilization time of 99% with GA and 0% with PSO. IAE_v was reduced by 50% with GA and by 48.1% with PSO. $ITAE_v$ was reduced by 48.3% with GA and by 44% with PSO. Note that the highest percentage reduction for all variables under analysis was achieved with the GA outperforming the PSO for the SBBC analyzed in this work.

Table 2. Summary of optimization results.

Variable	Result	Without Optimization	Optimization with GA	Optimization with PSO	Reduction with GA (%)	Reduction with PSO (%)
Input current	overshoot	11.18	8.48	9.5	24.15	15
	IAE_i	3362	3141	3235	6.6	3.8
	$ITAE_i$	117.6	108.5	109.1	7.7	7.2
Output voltage	Time (s)	0.43	0.0042	0.43	99	0
	IAE_v	16,222	8121	8327	50	48.1
	$ITAE_v$	511	264	287.5	48.3	44
Fitness function		4.831	3764	4400	22	9

5. Experimental Results

The validation of the optimization for control tuning is conducted using the SBBC device presented in Figure 22, and its features are listed in Table 3. This power electronics device was developed by the research group GIMEL at Universidad de Antioquia. A summary of the main Printed Circuit Boards (PCBs) of the SBBC is described below:

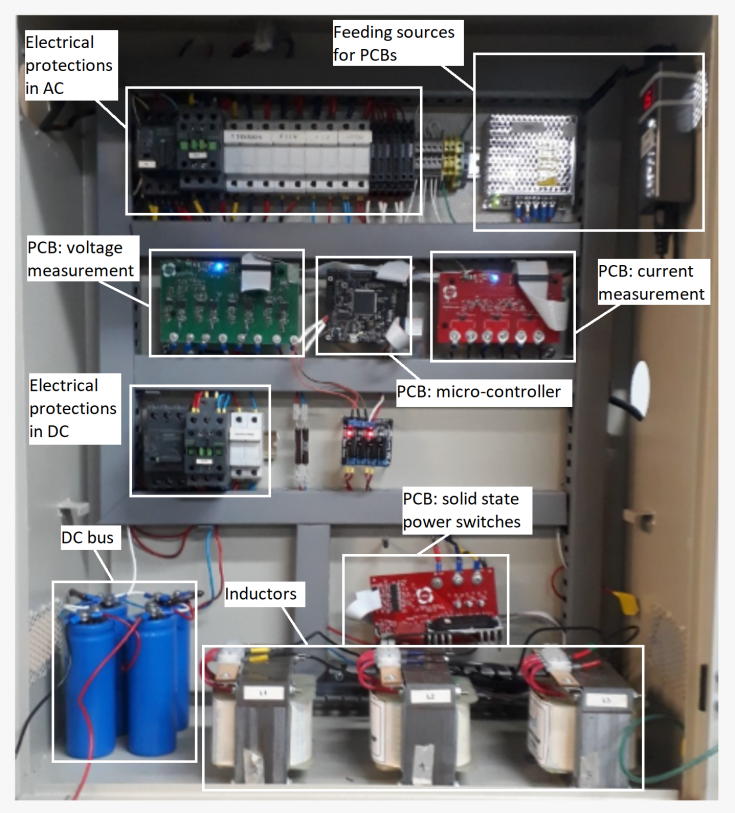

Figure 22. SBBC used for the validation of control and optimization.

Table 3. Features of the SBBC

Parameter	Value
Grid voltage (v_s)	12 Vrms, 60 Hz
DC bus capacitor (C)	2.200 µF
DC bus voltage (V_o)	40 V
Inductors ($L_1 = L_2 = L$)	2.3 mH
Switching frequency (f_{sw})	40 kHz
Load (R)	108 Ω

5.1. PCB: Micro-Controller

The PCB for Digital Signal Processing (DSP) and control was developed using a real-time micro-controller IC, the 32-Bit Single-Core TMS320F28335PGFA from Texas Instruments. The PCB was designed with inputs for voltage and current measurements, a port for serial communication, outputs to actuate relays, and power solid-state switches. Additionally, this micro-controller has libraries that focus on renewable energies and power electronics applications. The algorithm employed to implement Sliding Mode Control (SMC) with Active Harmonic Compensation (AHB) is depicted in Figure 23. The key steps of this algorithm are outlined below: (1) Measure currents and voltages. (2) Utilize the Phase-Locked Loop (PLL) to synchronize the system with the AC power supply. (3) Calculate the Sliding Surface and Adaptive Band utilizing the measurements from step 1 along with reference values. (4) Compare the values of the Sliding Surface and Adaptive Band. This comparison employs auxiliary variables: Rflip and Sflip (inputs), and Qflip and Qnflip (outputs). This arrangement emulates a RS flip-flop in accordance with Figure 9. (5) Control signals for both switches (IGBT1 and IGBT2) are activated to close the switches or deactivated to open them. Throughout this process, the sliding surface remains within the adaptive band.

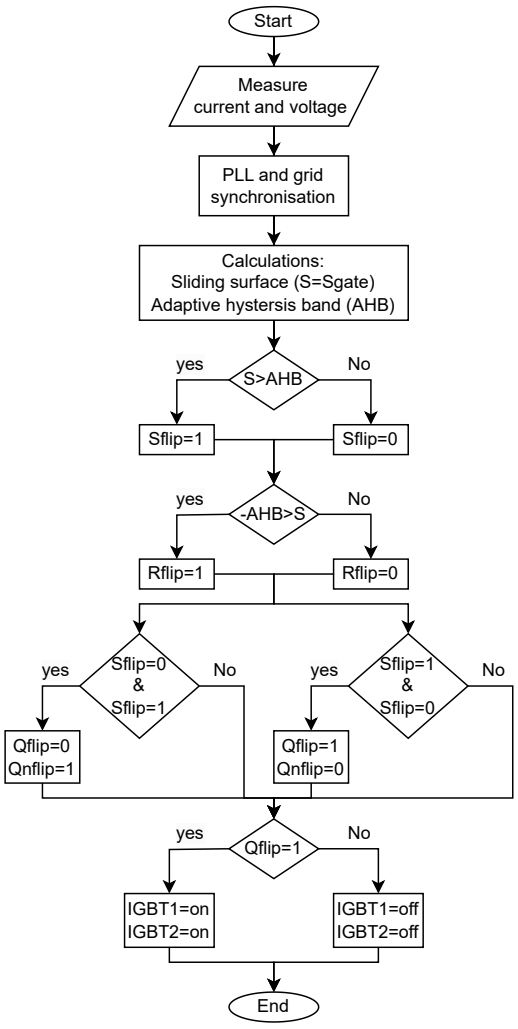

Figure 23. Control algorithm.

5.2. PCB: Measurement of Voltages and Currents

The PCB for current measurement has sensors ACS714, is fed with 5 Vdc, and can measure up to 10 Arms per channel. The PCB for voltage measurement has sensors AMC1200 and is fed by 5 Vdc and can measure up to 100 Vpeak per channel.

5.3. PCB: Solid State Power Switches

This board has a power module IRAM136-3063 (30 A, 600 V) as the main component composed of six Insulated-Gate Bipolar Transistors (IGBTs), with diode blocking voltage and integrated gate drivers. This PCB is fed by 15 Vdc.

5.4. First Test: Control without Optimization

Figure 24 presents the experimental results with $\alpha_1 = \alpha_2 = \alpha_3 = 1$ without optimization. The measurements were taken with a digital oscilloscope ROHDE & SCHWARZ RTH1004. The DC bus voltage (red) is 31.34 V, with the reference voltage being 30 V. The input current (green) is in phase with the input voltage (yellow), validating the PFC without optimization. However, in some cases, the current in negative half-cycles is not completely sinewave, with a value of 1.152 Arms.

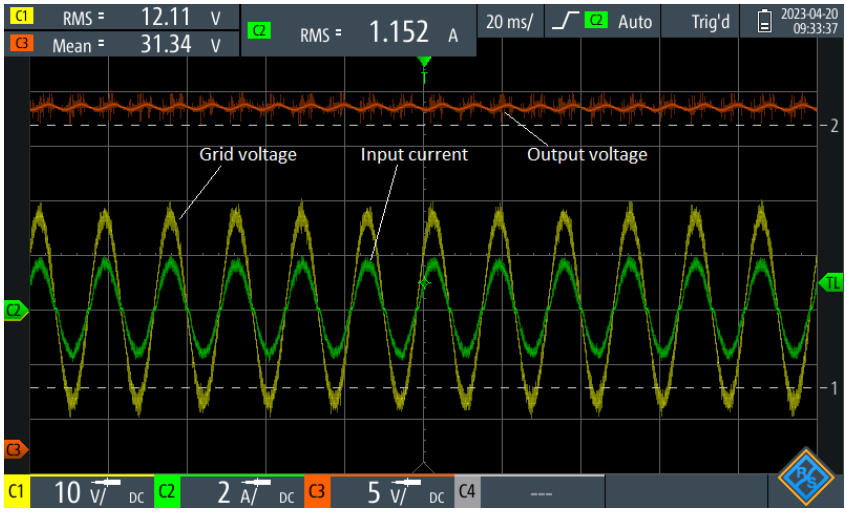

Figure 24. Experimental results: SMC with $\alpha_1 = \alpha_2 = \alpha_3 = 1$.

Figure 25 presents the control behavior in the face of disturbances. Figure 25a shows the response when the load is doubled; a resistance with the same values is connected in parallel. The voltage amplitude is reduced to 31.71 V, and the current increases to 2.45 Arms. Figure 25b illustrates the response when the reference voltage is changed from 30 V to 32 V. The output voltage stabilizes at 33.73 V with a stabilization time t = 1.2 s (slow response), with the reference set at 30 V. Basically, the control stabilizes and ensures PFC. However, the references are not correctly followed.

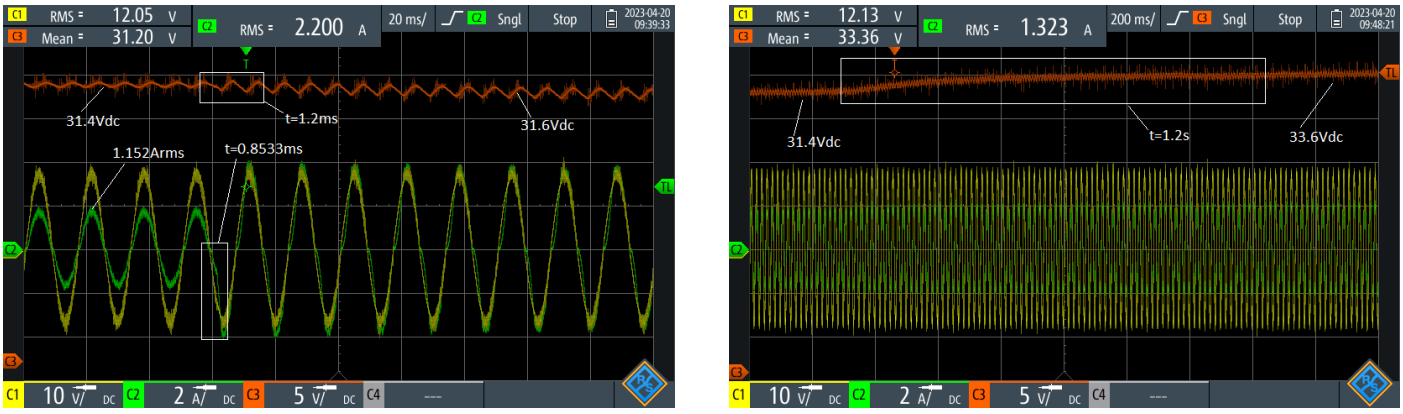

(**a**) (**b**)

Figure 25. Validation of adequate control behavior: (**a**) load change, (**b**) reference voltage change.

5.5. Second Test: Load Change with Optimization

Figure 26 presents the experimental results when the load is doubled with the sliding coefficients found with GA (Figure 26a) and PSO (Figure 26b) techniques. The output voltage presents an increase in the oscillations when the load is doubled for both cases. Nevertheless, the mean value according to the reference (30 V) is correctly followed in both cases, in contrast to results without optimization (Figure 25a); the voltage has a slight undershot only in the transient for PSO technique. Both GA and PSO techniques present an instantaneous response for the input current change.

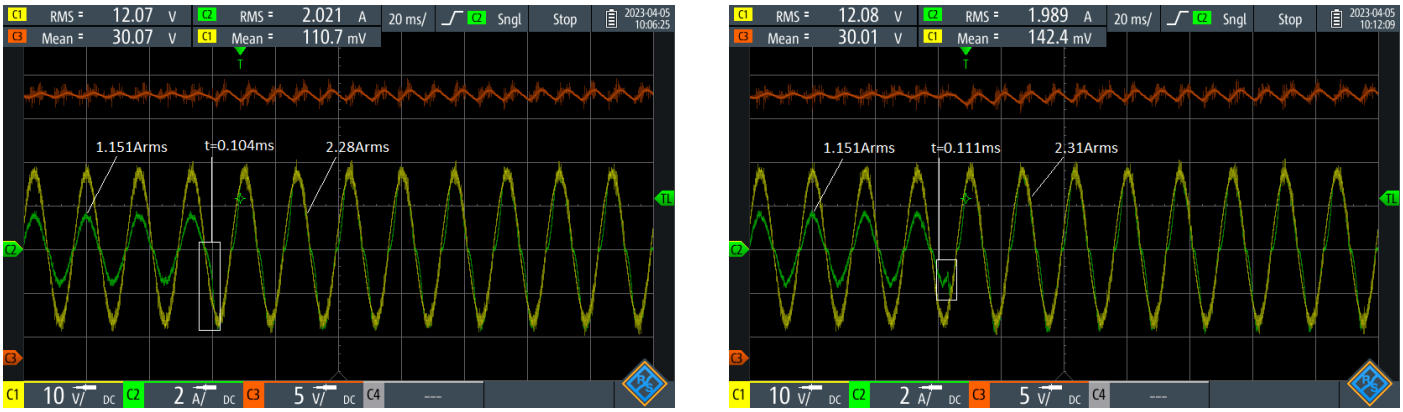

(**a**) (**b**)

Figure 26. Validation of adequate control behavior in the face of load change with optimization. (**a**) Load change with GA: $\alpha_1 = 10.65$, $\alpha_2 = 1.5$, $\alpha_3 = 12.7$; (**b**) Load change with PSO: $\alpha_1 = 13.21$, $\alpha_2 = 1.24$, $\alpha_3 = 5.34$.

5.6. Third Test: Reference Change

Figure 27 presents the experimental results when the reference voltage is changed from 30 V to 32 V with the sliding coefficients found with GA (Figure 27a) and PSO (Figure 27b) techniques. The output voltage presents the same behavior when the reference is changed. Nevertheless, PSO presents a slight peak (6.5%) in current, greater than the one from the GA (without peak), while the current with PSO reaches the nominal value two cycles later. Therefore, tuning with a GA has a better response than the one with a PSO.

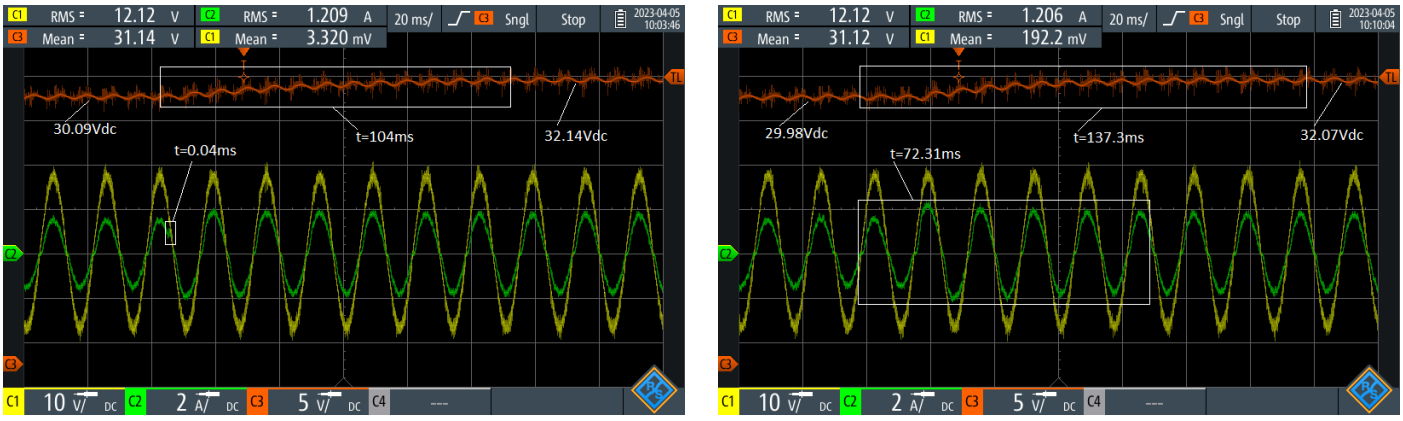

(**a**) (**b**)

Figure 27. Validation of adequate control behavior in the face of reference voltage change. (**a**) Reference change with GA: $\alpha_1 = 10.65$, $\alpha_2 = 1.5$, $\alpha_3 = 12.7$; (**b**) reference change with PSO: $\alpha_1 = 13.21$, $\alpha_2 = 1.24$, $\alpha_3 = 5.34$.

5.7. Detailed Data and Result Analysis

Table 4 presents the detailed data of experimental results. The first column exhibits the disturbance type (current in the second row and voltage in the third row). In this case, "time" corresponds to the stabilization time after disturbances. Results for the current present its RMS value and ripple before and after disturbances, with load doubled in this case. Results for the voltage present its mean value and oscillations (around the mean value) before and after disturbances, with reference change in this case. The fifth column shows the improvement percentage with the GA technique in regard to control without optimization (before and after). The sixth column with PSO technique respect to control without optimization (before and after). As a summary, the highest percentages of improvement in each case (GA and PSO) are highlighted in *italics*. The main conclusions for each test are shown below:

- Input current (load change): The stabilization time had an improvement of 87.34% with GA and 86.99% with PSO. Both optimizations had similar behavior. The value of current before disturbance did not have a significant change. Nevertheless, after load change, the current had a reduction (improvement) of 6.17% with GA and 4.93% with PSO. For both GA and PSO, the ripple before the disturbance presented a reduction of approximately 40%, and after the disturbance, a reduction of 24.08%. The load change portrayed a similar behavior for both metaheuristics, improving response speed (mainly stabilization time) considerably with respect to control without optimization.
- Output voltage (reference change): The stabilization time had an improvement of 91.03% with GA and 88.55% with PSO. The voltage followed the reference for both GA and PSO before (mean value of 30 V approximately) and after (mean value of 32 V approximately) the reference change in contrast to control without optimization, presenting an average improvement of 4.25% with GA and 4.53% with PSO. The oscillations around the reference voltage before the disturbance presented a reduction of 15.68% with GA and 7.92% with PSO. The oscillations after the disturbance presented a reduction of 35.21% with GA and 32.63% with PSO. The output voltage response was significantly improved with both metaheuristics. Nonetheless, PSO presented a significantly slow response for the input current when the voltage reference was changed as shown in Figure 27b where the current had a delay of 72.31 ms in comparison with Figure 27a (GA), where the current reached its stabilization value instantaneously.

Table 4. Experimental results (the highest percentages of improvement are indicated in *italics*).

Disturbance	Result	Without Optimization	Optimization with GA	Optimization with PSO	Improvement with GA(%)	Improvement with PSO(%)
Load change (Current)	time (ms)	0.8533	0.104	0.111	*87.34*	86.99
	value (Arms)	1.152–2.43	1.151–2.28	1.151–2.31	*0.087–6.17*	*0.087*–4.93
	ripple (mA)	507.7–526.9	303–400	307.7–400	*40.31–24.08*	39.39–*24.08*
Ref change (Voltage)	time (ms)	1.200	104	137.3	*91.03*	88.55
	mean value (V)	31.4–33.6	30.09–32.14	29.98–32.07	4.17–4.34	*4.52–4.55*
	oscillations (V)	0.593–1.633	0.5–1.058	0.546–1.1	*15.68–35.21*	7.92–32.63

6. Conclusions

This paper presented the implementation and comparison of two metaheuristic approaches (GA and PSO) applied to improve the behavior of a SBBC with a PFC controlled by SMC. Both metaheuristic techniques were coded in Python, while the SBBC circuit was built and simulated in OpenModelica. The data was obtained through Python from OpenModelica, and the metaheuristics assessed the fitness function using an interface. The fitness function was built with the performance indexes IAE and ITAE for the input current and the output voltage to minimize the errors between the measured data and their

respective references. IAE penalized errors in the start-up, while ITAE penalized errors in the steady state. The sliding coefficients were conceived as decision variables, consequently obtaining the best tuning for the SMC controller. The optimization process takes the circuit in OpenModelica as a black box model and computes the results by processing the measured data. Simulation results evidenced that the GA featured a better performance for all variables under analysis. The GA presented a reduction in the fitness function of approximately 22%, with a reduction in the input current overshoot of up to 24,15% in the start-up and a reduction in the setting time of up to 99% for the output voltage, giving a better result than PSO in this case. The priority to obtain a better performance for either the current or voltage can be selected from the fitness function by modifying the weights according to desired requirements. In this case, the current was given priority in the optimization process, since it presented a great overshoot in the start-up. The validation with experimental results showed similar behavior for both metaheuristics; in the steady state, the converter's behavior with GA and PSO is the same; nevertheless, tuning with a GA presents a better response in the face of disturbances than tuning with a PSO.

Author Contributions: Conceptualization, J.R.O.-C., J.B.C.-Q., N.M.-G., S.D.S.-Z. and J.M.L.-L.; Data curation, J.R.O.-C.; Formal analysis, J.R.O.-C., J.B.C.-Q., N.M.-G., S.D.S.-Z. and J.M.L.-L.; Funding acquisition, J.M.L.-L., J.B.C.-Q. and N.M.-G.; Investigation, J.R.O.-C., J.B.C.-Q., N.M.-G., S.D.S.-Z. and J.M.L.-L.; Methodology, J.R.O.-C., J.B.C.-Q., N.M.-G., S.D.S.-Z. and J.M.L.-L.; Project administration, S.D.S.-Z. and N.M.-G.; Resources, S.D.S.-Z., N.M.-G. and J.M.L.-L.; Software, J.R.O.-C.; Supervision, N.M.-G. and J.M.L.-L.; Validation, J.R.O.-C.; Test, J.R.O.-C., S.B.-C.; Visualization, J.R.O.-C., J.B.C.-Q., N.M.-G., S.D.S.-Z. and J.M.L.-L.; Writing—original draft, J.R.O.-C.; Writing—review and editing, J.R.O.-C., J.B.C.-Q., N.M.-G., S.D.S.-Z. and J.M.L.-L. All authors have read and agreed to the published version of the manuscript.

Funding: This research was funded in part by the Colombia Scientific Program within the framework of the call Ecosistema Científico (Contract No. FP44842-218-2018). The authors also thank "Institución Universitaria Pascual Bravo" for its financial support under the "Talento Pascualino" program.

Data Availability Statement: Not applicable.

Acknowledgments: The authors gratefully acknowledge the support from the Colombia Scientific Program within the framework of the call Ecosistema Científico (Contract No. FP44842- 218-2018). The authors also want to acknowledge Universidad de Antioquia for its support through the project "Estrategia de Sostenibilidad". The authors gratefully acknowledge the support from "Institución Universitaria Pascual Bravo" through the project "Talento Pascualino". The authors are also grateful to Paula Andrea Gil for her help with the PCB reparations.

Conflicts of Interest: The authors declare no conflict of interest.

References

1. Komurcugil, H.; Biricik, S.; Bayhan, S.; Zhang, Z. Sliding Mode Control: Overview of Its Applications in Power Converters. *IEEE Ind. Electron. Mag.* **2021**, *15*, 40–49. [CrossRef]
2. Mehta, A.; Naik, B. Sliding Mode Controllers for Power Electronic Converters. In *Lecture Notes in Electrical Engineering*; Springer: Singapore, 2019; Volume 534. [CrossRef]
3. Rayane, K.; Bougrine, M.; Benalia, A.; Guesmi, K. Sliding Mode Control of a Three-Phase Inverter with an Output LC Filter. In Proceedings of the 2018 International Conference on Applied Smart Systems (ICASS), Medea, Algeria, 24–25 November 2018; pp. 1–4. [CrossRef]
4. Afshar, Z.; Zadeh, M.M.; Bathaee, S.M.T. Sliding Mode Control of Grid-connected Inverters Using Inverter Output Current. In Proceedings of the 2019 IEEE International Conference on Environment and Electrical Engineering and 2019 IEEE Industrial and Commercial Power Systems Europe (EEEIC / I&CPS Europe), Genova, Italy, 11–14 June 2019; pp. 1–5. [CrossRef]
5. Gulbudak, O.; Gokdag, M.; Komurcugil, H. Dual-sliding mode control of nine-switch inverter. *Int. Trans. Electr. Energy Syst.* **2021**, *31*, e13185. [CrossRef]
6. Srinivasan, S.; Arivukkannu, E.; Muthiah, R. A fuzzy sliding mode controller for power quality improvement of solar PV interleaved parallel inverters in a micro-grid. *Int. J. Ambient. Energy* **2022**, *43*, 8386–8399. [CrossRef]
7. Mohammadhassani, F.; Gholizade Narm, H. Control of a Single Stage Boost Inverter Based on Dynamic Sliding Mode Control with Power Decoupling. *Int. J. Eng.* **2020**, *33*, 1978–1985. [CrossRef]

8. Awais, M.; Yasin, A.R.; Riaz, M.; Saqib, B.; Zia, S.; Yasin, A. Robust Sliding Mode Control of a Unipolar Power Inverter. *Energies* **2021**, *14*, 5405. [CrossRef]
9. Hou, B.; Liu, J.; Dong, F.; Wang, M.; Mu, A. Sliding mode control strategy of voltage source inverter based on load current sliding mode observer. In Proceedings of the 2016 IEEE 8th International Power Electronics and Motion Control Conference (IPEMC-ECCE Asia), Hefei, China, 22–26 May 2016; pp. 1269–1273. [CrossRef]
10. Sira-Ramirez, H. Nonlinear variable structure systems in sliding mode: The general case. *IEEE Trans. Autom. Control* **1989**, *34*, 1186–1188. [CrossRef]
11. Chincholkar, S.H.; Jiang, W.; Chan, C.Y. A Normalized Output Error-Based Sliding-Mode Controller for the DC–DC Cascade Boost Converter. *IEEE Trans. Circuits Syst. II Express Briefs* **2020**, *67*, 92–96. [CrossRef]
12. Sira-Ramirez, H.; Rios-Bolivar, M. Sliding mode control of DC-to-DC power converters via extended linearization. *IEEE Trans. Circuits Syst. I Fundam. Theory Appl.* **1994**, *41*, 652–661. [CrossRef]
13. Singh, P.; Purwar, S. Sliding mode controller for PWM based Buck-Boost DC/DC converter as state space averaging method in continuous conduction mode. In Proceedings of the 2012 2nd International Conference on Power, Control and Embedded Systems, Allahabad, India, 17–19 December 2012; pp. 1–5. [CrossRef]
14. Sira-Ramírez, H. On the generalized PI sliding mode control of DC-to-DC power converters: A tutorial. *Int. J. Control.* **2003**, *76*, 1018–1033. [CrossRef]
15. Strzelecki, R.; Zinoviev, G.S. Overview of Power Electronics Converters and Controls. In *Power Electronics in Smart Electrical Energy Networks*; Strzelecki, R.M., Benysek, G., Eds.; Springer: London, UK, 2008; pp. 55–105. [CrossRef]
16. Can, E. The design and experimentation of the new cascaded DC-DC boost converter for renewable energy. *Int. J. Electron.* **2019**, *106*, 1374–1393. [CrossRef]
17. Can, E. PWM controlling of a new multi DC-DC converter circuit. *Teh. Glas.* **2019**, *13*, 116–122. [CrossRef]
18. Can, E.; Toksoy, M.S. A flexible closed-loop (fcl) pid and dynamic fuzzy logic + pid controllers for optimization of dc motor. *J. Eng. Res.* **2023**, *11*, 1A. [CrossRef]
19. Garduño, D.M.; Rivas, J.J.R.; Castillo, O.C.; González, R.O.; Gutiérrez, F.E.R. Current Distortion Rejection in PMSM Drives Using an Adaptive Super-Twisting Algorithm. *IEEE Trans. Energy Convers.* **2022**, *37*, 927–934. [CrossRef]
20. Mlakić, D.; Baghaee, H.R.; Nikolovski, S. A Novel ANFIS-Based Islanding Detection for Inverter-Interfaced Microgrids. *IEEE Trans. Smart Grid* **2019**, *10*, 4411–4424. [CrossRef]
21. Yang, Z.; Zeng, J.; Zhang, Q.; Zhang, Z.; Winstead, V.; Yu, D. A Composite Power Decoupling Method for a PV Inverter With Optimized Energy Buffer. *IEEE Trans. Ind. Appl.* **2021**, *57*, 3877–3887. [CrossRef]
22. di Benedetto, M.; Lidozzi, A.; Solero, L.; Crescimbini, F.; Grbović, P.J. Five-Level E-Type Inverter for Grid-Connected Applications. *IEEE Trans. Ind. Appl.* **2018**, *54*, 5536–5548. [CrossRef]
23. Pérez Posada, A.F.; Villegas, J.G.; López-Lezama, J.M. A Scatter Search Heuristic for the Optimal Location, Sizing and Contract Pricing of Distributed Generation in Electric Distribution Systems. *Energies* **2017**, *10*, 1449. [CrossRef]
24. Agudelo, L.; López-Lezama, J.M.; Muñoz-Galeano, N. Vulnerability assessment of power systems to intentional attacks using a specialized genetic algorithm. *Dyna* **2015**, *82*, 78–84. [CrossRef]
25. Saldarriaga-Zuluaga, S.D.; López-Lezama, J.M.; Muñoz-Galeano, N. An Approach for Optimal Coordination of Over-Current Relays in Microgrids with Distributed Generation. *Electronics* **2020**, *9*, 1740. [CrossRef]
26. Dracopoulos, D.C., Genetic Algorithms and Genetic Programming for Control. In *Evolutionary Algorithms in Engineering Applications*; Springer: Berlin/Heidelberg, Germany, 1997; pp. 329–343. [CrossRef]
27. Wang, Q.; Spronck, P.; Tracht, R. An overview of genetic algorithms applied to control engineering problems. In Proceedings of the 2003 International Conference on Machine Learning and Cybernetics (IEEE Cat. No.03EX693), Xi'an, China, 5 November 2003; Volume 3, pp. 1651–1656. [CrossRef]
28. Fleming, P.; Fonseca, C. Genetic Algorithms in Control Systems Engineering. In Proceedings of the 12th Triennal Wold Congress of the International Federation of Automatic Control Volume 2 Robust Control, Design and Software, Sydney, Australia, 18–23 July 1993; Volume 26, pp. 605–612. [CrossRef]
29. Varsek, A.; Urbancic, T.; Filipic, B. Genetic algorithms in controller design and tuning. *IEEE Trans. Syst. Man Cybern.* **1993**, *23*, 1330–1339. [CrossRef]
30. Zulu, M.L.T.; Carpanen, R.P.; Tiako, R. A Comprehensive Review: Study of Artificial Intelligence Optimization Technique Applications in a Hybrid Microgrid at Times of Fault Outbreaks. *Energies* **2023**, *16*, 1786. [CrossRef]
31. Nappu, M.B.; Arief, A.; Ajami, W.A. Energy Efficiency in Modern Power Systems Utilizing Advanced Incremental Particle Swarm Optimization-Based OPF. *Energies* **2023**, *16*, 1706. [CrossRef]
32. AlRashidi, M.R.; AlHajri, M.F.; Al-Othman, A.K.; El-Naggar, K.M. Particle Swarm Optimization and Its Applications in Power Systems. In *Computational Intelligence in Power Engineering*; Springer: Berlin/Heidelberg, Germany, 2010; pp. 295–324. [CrossRef]
33. Dell'Aquila, A.; Lecci, A. PSO-based control optimization of power converters. In Proceedings of the 2008 International Symposium on Power Electronics, Electrical Drives, Automation and Motion, Ischia, Italy, 11–13 June 2008; pp. 964–968. [CrossRef]
34. Zhang, J.; Shi, Y.; Zhan, Z.H. Power Electronic Circuits Design: A Particle Swarm Optimization Approach. In Proceedings of the Simulated Evolution and Learning, Berlin, Germany, 7–10 December 2008; pp. 605–614.

35. Eswaran, T.; Kumar, V.S. Particle swarm optimization (PSO)-based tuning technique for PI controller for management of a distributed static synchronous compensator (DSTATCOM) for improved dynamic response and power quality. *J. Appl. Res. Technol.* **2017**, *15*, 173–189. [CrossRef]
36. Achiammal, B.; Kayalvizhi, D.R. Optimal Tuning of PI Controller Using Genetic Algorithm for Power Electronic Converter. *Int. J. Eng. Res. Technol.* **2013**, *2*, 6. [CrossRef]
37. Choi, Y.K.; Jung, B.W. Parameter Tuning for Buck Converters Using Genetic Algorithms. In *Advanced Intelligent Computing Theories and Applications: With Aspects of Artificial Intelligence*; Huang, D.S., Heutte, L., Loog, M., Eds.; Springer: Berlin/Heidelberg, Germany, 2007; pp. 641–647.
38. Ghassani, R.; Bratcu, A.I.; Teodorescu, R. Genetic Algorithm Applied to State-Feedback Control Design of Grid and Circulating Current in Modular Multilevel Converters. *IFAC-Pap.* **2022**, *55*, 431–436. [CrossRef]
39. Mejía-Ruiz, G.E.; Muñoz-Galeano, N.; López-Lezama, J.M. Modeling and development of a bridgeless PFC Boost rectifier. *Rev. Fac. De Ing. Univ. Antioq.* **2017**, *82*, 9–21. [CrossRef]
40. Aamir, M.; Mekhilef, S. An Online Transformerless Uninterruptible Power Supply (UPS) System With a Smaller Battery Bank for Low-Power Applications. *IEEE Trans. Power Electron.* **2017**, *32*, 233–247. [CrossRef]
41. *IEC 61000-3-2*; IEC Electromagnetic Compatibility (EMC)—Part 3-2: Limits for Harmonic Current Emissions. IEC: Geneva, Switzerland, 2021; pp. 1–28.
42. *IEEE P519/D5.1*; IEEE Draft Standard for Harmonic Control in Electric Power Systems. IEEE: Washington, DC, USA, 2021; pp. 1–30.
43. Ancuti, M.C.; Svoboda, M.; Musuroi, S.; Hedes, A.; Olarescu, N.V. Boost PFC converter versus bridgeless boost PFC converter EMI analysis. In Proceedings of the 2014 International Conference on Applied and Theoretical Electricity (ICATE), Craiova, Romania, 23–25 October 2014; pp. 1–6. [CrossRef]
44. Tseng, S.Y.; Fan, J.H. Bridgeless Boost Converter with an Interleaving Manner for PFC Applications. *Electronics* **2021**, *10*, 296. [CrossRef]
45. Musavi, F.; Eberle, W.; Dunford, W.G. A Phase-Shifted Gating Technique with Simplified Current Sensing for the Semi-Bridgeless AC–DC Converter. *IEEE Trans. Veh. Technol.* **2013**, *62*, 1568–1576. [CrossRef]
46. Mejía-Ruiz, G.E.; Muñoz-Galeano, N.; Ortiz-Castrillón, J.R. Banda de Histéresis Adaptativa para un Convertidor AC-DC Elevador sin Puente, con Correccion del Factor de Potencia y Control por Modos Deslizantes. *Inform. Tecnol.* **2019**, *30*, 283–292. [CrossRef]
47. Ortiz-Castrillón, J.R.; Mejía-Ruiz, G.E.; Muñoz-Galeano, N.; López-Lezama, J.M.; Cano-Quintero, J.B. A Sliding Surface for Controlling a Semi-Bridgeless Boost Converter with Power Factor Correction and Adaptive Hysteresis Band. *Appl. Sci.* **2021**, *11*, 1873. [CrossRef]
48. Ahmed, M.; Ebrahim, M.; Ramadan, H.; Becherif, M. Optimal Genetic-sliding Mode Control of VSC-HVDC Transmission Systems. *Energy Procedia* **2015**, *74*, 1048–1060. [CrossRef]
49. Terán-Picón, J.C.; Anderez, J.; Camacho, O. Genetics algorithms as a tuning tool for PID and sliding mode controllers. *Rev. Técnica La Fac. Ing. Univ. Del Zulia* **2005**, *28*, 200–209.
50. Köse, E.; Abaci, K.; Kizmaz, H.; Aksoy, S.; Yalçin, M.A. Sliding Mode Control Based on Genetic Algorithm for WSCC Systems Include of SVC. *Elektron. Elektrotechnika* **2013**, *19*, 25–28. [CrossRef]
51. Tiwari, S.; Rayeen, Z.; Hanif, O. Design and Analysis of Fractional Order PID Controller tuning via Genetic Algorithm for CUK Converter. In Proceedings of the 2018 IEEE 13th International Conference on Industrial and Information Systems (ICIIS), Rupnagar, India, 1–2 December 2018; pp. 436–441. [CrossRef]
52. Alfergani, A.; Elkawafi, S.; Nour, T.M.; Mohamed Elkezza, K.; Kahlil, A. Performance Evaluation of DC-DC Buck Converter with Voltage Control Loop Using Genetic Algorithm with Different Objective Functions. In Proceedings of the 2023 IEEE 3rd International Maghreb Meeting of the Conference on Sciences and Techniques of Automatic Control and Computer Engineering (MI-STA), Benghazi, Libya, 21–23 May 2023; pp. 135–140. [CrossRef]
53. Bonyadi, M.R.; Michalewicz, Z. Particle Swarm Optimization for Single Objective Continuous Space Problems: A Review. *Evol. Comput.* **2017**, *25*, 1–54. [CrossRef]
54. Kennedy, J.; Eberhart, R. Particle swarm optimization. In Proceedings of the ICNN'95–International Conference on Neural Networks, Perth, Australia, 6 August 1995; Volume 4, pp. 1942–1948. [CrossRef]

Disclaimer/Publisher's Note: The statements, opinions and data contained in all publications are solely those of the individual author(s) and contributor(s) and not of MDPI and/or the editor(s). MDPI and/or the editor(s) disclaim responsibility for any injury to people or property resulting from any ideas, methods, instructions or products referred to in the content.